

The effects of short-lived radionuclides and porosity on the early thermo-mechanical evolution of planetesimals

Tim Lichtenberg^{a,b,*}, Gregor J. Golabek^{b,c}, Taras V. Gerya^b, Michael R. Meyer^a

^a*Institute for Astronomy, ETH Zürich, Wolfgang-Pauli-Strasse 27, 8093 Zürich, Switzerland*

^b*Institute of Geophysics, ETH Zürich, Sonneggstrasse 5, 8092 Zürich, Switzerland*

^c*Bayerisches Geoinstitut, University of Bayreuth, Universitätsstrasse 30, 95440 Bayreuth, Germany*

Abstract

The thermal history and internal structure of chondritic planetesimals, assembled before the giant impact phase of chaotic growth, potentially yield important implications for the final composition and evolution of terrestrial planets. These parameters critically depend on the internal balance of heating versus cooling, which is mostly determined by the presence of short-lived radionuclides (SLRs), such as ^{26}Al and ^{60}Fe , as well as the heat conductivity of the material. The heating by SLRs depends on their initial abundances, the formation time of the planetesimal and its size. It has been argued that the cooling history is determined by the porosity of the granular material, which undergoes dramatic changes via compaction processes and tends to decrease with time. In this study we assess the influence of these parameters on the thermo-mechanical evolution of young planetesimals with both 2D and 3D simulations. Using the code family `i2ELVIS/i3ELVIS` we have run numerous 2D and 3D numerical finite-difference fluid dynamic models with varying planetesimal radius, formation time and initial porosity. Our results indicate that powdery materials lowered the threshold for melting and convection in planetesimals, depending on the amount of SLRs present. A subset of planetesimals retained a powdery surface layer which lowered the thermal conductivity and hindered cooling. The effect of initial porosity was small, however, compared to those of planetesimal size and formation time, which dominated the thermo-mechanical evolution and were the primary factors for the onset of melting and differentiation. We comment on the implications of this work concerning the structure and evolution of these planetesimals, as well as their behavior as possible building blocks of terrestrial planets.

Keywords: Planetary formation, Terrestrial planets, Planetesimals, Interiors, Thermal histories

1. Introduction

During the early stages of planet formation the building material of terrestrial planets like Earth or Mars is distributed within planetesimals with sizes of $\sim 10^1\text{--}10^2$ km (Weidenschilling and Cuzzi, 2006). It remains unclear how these bodies assembled from sub-micron grains in a circumstellar disk in detail. First order constraints from the standard collisional model for growth relate the doubling time $t_s \sim \rho_p R_p / (\Sigma_{\text{disk}} \Omega_K)$ of a growing planetesimal to its size R_p and density ρ_p as well as to the properties of the disk, namely mass surface density Σ_{disk} and Keplerian frequency Ω_K (Goldreich et al., 2004). This formula, however, essentially a cross-section calculation, ignores gravitational focusing and limits to growth, such as the bouncing barrier (e.g., Zsom et al., 2010) and the radial migration of solids due to gas drag (Weidenschilling, 1977). Nonetheless, there are also complex local processes that can enhance the formation of planetesimals with up to several hundred kilometers radii due to particle collection in vortices, pressure bumps, and other effects (e.g., Johansen et al., 2007; Cuzzi et al., 2008; Morbidelli et al., 2009; Chambers, 2010; Johansen et al., 2015). These point to rapid formation on the time scale of $\sim 10^5$ yr after the formation of Ca-Al-rich inclusions (CAIs), consistent with findings

from geochemical data (Kleine et al., 2009).

Theoretical models to investigate this epoch after the initial assembly of the planetesimals rely on numerical models of internal dynamics. So far, such models were mostly based on 1D studies, focusing on conductive cooling as the main heat transfer mechanism (e.g., Ghosh and McSween, 1998; Hevey and Sanders, 2006; Sahijpal et al., 2007). Recent work, however, has shown that more mechanisms need to be taken into account. Firstly, these bodies are supposed to be sufficiently big to become heated by decay of short-lived radionuclides (SLRs), most importantly ^{26}Al and ^{60}Fe , which would alter their inner structure and evolution dramatically up to the point of silicate melting. For example, bodies greater than ~ 10 km in radius, formed at the time of CAI formation, are supposed to melt completely (Hevey and Sanders, 2006). Secondly, some meteorite parent bodies seem to have experienced solid-state deformation (Tkalcic et al., 2013; Tkalcic and Brenker, 2014). These points underline the importance of 2D or 3D thermo-mechanical modeling approaches for the evolution of planetesimals to detect effects such as the differences of the surface-to-volume ratio in 1D, 2D and 3D models or non-axisymmetric advection processes. As a further complicating issue, recent work highlights the potentially important role of porous bulk material on the thermal history of planetesimals, by lowering the thermal conductivity of the silicate material and thus to prevent effective

*Corresponding author. E-mail: tim.lichtenberg@phys.ethz.ch.

heat transport via conduction (Cuzzi et al., 2008; Neumann et al., 2014).

The initial powdery state of the uncompact material is however reduced in the inner parts of the planetesimals by cold isostatic compaction due to self-gravity (Henke et al., 2012), effectively decreasing its influence with increasing size of the body. Another important aspect is the formation time of the body. As outlined above, the accretion time scale of planetesimals is on the order of 10^5 yr, which is roughly an order of magnitude shorter than the evolutionary time scale of the protoplanetary disk and the thermo-mechanical evolution of planetesimals on the order of 10^6 yr. Hence, the quasi-instantaneous formation time sets the limit on the amount of SLRs incorporated into the body.

Additional heat sources for planetesimals can be energy injection during the accretion of the body and later impacts. First, the temperature increase due to the conversion of gravitational energy to heat is low for bodies < 1000 km (Schubert et al., 1986; Qin et al., 2008; Elkins-Tanton et al., 2011). Second, during runaway growth, the velocity dispersion of planetesimals is set by the equilibrium between self-stirring and gas drag. Impact velocities are therefore comparable or smaller to the escape velocity (Greenberg et al., 1978; Morbidelli et al., 2015), which drastically limits the amount of injected energy. The formation time thus dominates the energy budget for heating and sets the pace of internal dynamic processes, such as core formation, to the order of several ^{26}Al half-lives.

Clearly, the thermo-mechanical evolution of planetesimals needs to be treated adequately to achieve a consistent theoretical understanding of this stage of planetary assembly. In this study we assessed the role of the initial size, formation time and porosity of planetesimals on their thermo-mechanical history via 2D and 3D numerical models. In Sect. 2 we describe constraints from earlier work and outline the most important concepts of our numerical model; in Sect. 3 we present the results obtained from the simulation runs, for which we outline the technically inherent limitations in Sect. 4. In Sect. 5 we discuss the physical implications and draw conclusions in Sect. 6. Supplementary material can be found in Appendix A and a list of all simulations is given in Appendix B.

2. Physical and numerical methodology

The physical and numerical methods in this work follow earlier work by Golabek et al. (2014), in which an in-depth analysis of observational constraints on the thermal history for the acapulcoite-lodranite parent body is compiled. In contrast to this study, we focused on the general role of planetesimal evolution and sought to explore the thermo-mechanical regimes before the onset of the giant impact phase in terrestrial planet formation. The most important physical constants used in the model are explained in the following sections, all others are listed with their respective references in Table 1.

2.1. Fluid flow

As outlined in Sect. 1 we studied the thermo-mechanical evolution of instantaneously and recently formed planetesimals

using the `i2ELVIS/i3ELVIS` code family (Gerya and Yuen, 2007). The code solves the fluid dynamic conservation equations using the extended Boussinesq approximation, to account for thermal and chemical buoyancy forces, with a conservative finite-differences (FD) approach on a fully staggered-grid (Gerya and Yuen, 2003), namely the continuity equation

$$\frac{\partial \rho}{\partial t} + \nabla \cdot \rho \mathbf{v} = 0, \quad (1)$$

with density ρ , time t and flow velocity \mathbf{v} ; the Stokes equation

$$\nabla \cdot \sigma' - \nabla P + \rho \mathbf{g} = 0, \quad (2)$$

with deviatoric stress tensor σ' , pressure P and directional gravity \mathbf{g} obtained via the location-dependent Poisson equation

$$\nabla^2 \Phi = 4\pi G \rho, \quad (3)$$

with the gravitational potential Φ and Newton's constant G ; and finally the energy equation

$$\rho c_p \left(\frac{\partial T}{\partial t} + \mathbf{v}_i \cdot \nabla T \right) = -\frac{\partial q_i}{\partial x_i} + H_r + H_s + H_L, \quad (4)$$

with heat capacity c_p , temperature T , heat flux $q_i = -k \frac{\partial T}{\partial x_i}$, thermal conductivity k , and radioactive (H_r), shear (H_s) and latent (H_L) heat production terms. The energy equation is advanced using a Lagrangian marker-in-cell technique to minimise numerical diffusion and enable an accurate advection of non-diffusive flow properties during material deformation. The staggered-grid FD method permits to capture sharp variations of stresses and thermal gradients with strongly variable viscosity and thermal conductivity. For further details on the code's features we refer to Gerya and Yuen (2003, 2007).

2.2. Heating by short-lived radionuclides

As discussed earlier, the radiogenic heat source term H_r in Equation 4 is dominant for early formed planetesimals. It is driven by the decay of short-lived isotopes ^{26}Al and ^{60}Fe and the long-lived ^{40}K , ^{235}U , ^{238}U and ^{232}Th . Among these ^{26}Al is by far the most important one and therefore drives the internal heating of the young bodies, as the abundance of ^{60}Fe is lower by orders of magnitude (Barr and Canup, 2008; Tang and Dauphas, 2012; Mishra et al., 2016). In this work, we considered time-dependent radiogenic heating by ^{26}Al and the long-lived radioactive isotopes as input for H_r in Equation 4. For the initial $^{26}\text{Al}/^{27}\text{Al}$ ratio we adopted an upper-limit value (Jacobsen et al., 2008) of $5.85 \cdot 10^{-5}$ (Thrane et al., 2006) at CAI formation.

2.3. Silicate melting model

For the silicates we assumed a peridotite composition and used the parameterizations by Herzberg et al. (2000) and Wade and Wood (2005) (based on data of Trønnes and Frost, 2002) for the solidus and liquidus temperatures T_{sol} and T_{liq} , which determine the silicate melt fraction

$$\varphi = \begin{cases} 0 & : T \leq T_{\text{sol}}, \\ \frac{T - T_{\text{sol}}}{T_{\text{liq}} - T_{\text{sol}}} & : T_{\text{sol}} < T < T_{\text{liq}}, \\ 1 & : T \geq T_{\text{liq}}. \end{cases} \quad (5)$$

PARAMETER	SYMBOL	VALUE	UNIT	REFERENCE
Density of uncompressed solid silicates	$\rho_{\text{Si-sol}}$	3500	kg m^{-3}	Stolper et al. (1981); Suzuki et al. (1998)
Density of uncompressed molten silicates	$\rho_{\text{Si-liq}}$	2900	kg m^{-3}	Stolper et al. (1981)
Temperature of space (sticky air)	T_{space}	290	K	Ghosh and McSween (1998); Barshay and Lewis (1976)
Activation energy	E_a	470	kJ mol^{-1}	Ranalli (1995)
Dislocation creep onset stress	σ_0	$3 \cdot 10^7$	Pa	Turcotte and Schubert (2014)
Power law exponent	n	4		Ranalli (1995)
Latent heat of silicate melting	L_{Si}	400	kJ kg^{-1}	Ghosh and McSween (1998); Turcotte and Schubert (2014)
Silicate melt fraction at rheological transition	φ_{crit}	0.4	non-dim.	Solomatov (2015); Costa et al. (2009)
Heat capacity of of silicates	c_p	1000	$\text{J kg}^{-1} \text{K}^{-1}$	Turcotte and Schubert (2014)
Thermal expansivity of solid silicates	$\alpha_{\text{Si-sol}}$	$3 \cdot 10^{-5}$	K^{-1}	Suzuki et al. (1998)
Thermal expansivity of molten silicates	$\alpha_{\text{Si-liq}}$	$6 \cdot 10^{-5}$	K^{-1}	Suzuki et al. (1998)
Thermal conductivity of solid silicates	k	3	$\text{W m}^{-1} \text{K}^{-1}$	Tarduno et al. (2012)
Thermal expansivity of molten silicates	k_{eff}	$\leq 10^6$	$\text{W m}^{-1} \text{K}^{-1}$	Golabek et al. (2014)
Minimum thermal conductivity of unsintered solid silicates	k_{low}	10^{-3}	$\text{W m}^{-1} \text{K}^{-1}$	Yomogida and Matsui (1984); Henke et al. (2012)
Temperature at onset of hot sintering	T_{sint}	700	K	Yomogida and Matsui (1984)

Table 1: List of physical parameters in the numerical model.

We took into account both consumption and release of latent heat due to melting and freezing of silicates. Silicate density depends on the melt fraction φ as

$$\rho_{\text{eff}}(P, T, \varphi) = \rho_{\text{Si-sol}}(P, T) \quad (6)$$

$$- \varphi[\rho_{\text{Si-sol}}(P, T) - \rho_{\text{Si-liq}}(P, T)] \quad (7)$$

with solid and liquid silicate densities $\rho_{\text{Si-sol}}$ and $\rho_{\text{Si-liq}}$. For silicate melt fractions $0.1 < \varphi \lesssim 0.4$ the effective viscosity (Pinkerton and Stevenson, 1992) is given as

$$\eta_{\text{eff}} = \eta_{\text{Si-liq}} \cdot \exp\left(\left[2.5 + \left(\frac{1-\varphi}{\varphi}\right)^{0.48}\right] \cdot (1-\varphi)\right). \quad (8)$$

Above $\varphi \gtrsim 0.4$ a transition occurs from solid-like structures to low-viscosity crystal suspensions (Solomatov, 2015; Costa et al., 2009), with $\eta_{\text{Si-liq}} = 10^{-4} - 10^2 \text{ Pa s}$ (Bottinga and Weill, 1972; Rubie et al., 2003; Liebske et al., 2005). This effectively increases the Rayleigh number

$$Ra = \frac{\alpha g (T - T_{\text{surf}}) \rho_{\text{eff}}^2 c_p D^3}{k \eta_{\text{Si-liq}}}, \quad (9)$$

with thermal expansivity α , surface temperature T_{surf} , depth of the magma ocean D and thermal conductivity k and thus enables an efficient cooling process.

Above melt fractions $\varphi \gtrsim 0.4$ our model is restricted by a lower cut-off viscosity $\eta_{\text{num}} = 10^{17} \text{ Pa s}$, which preserves numerical stability, but lies orders of magnitude above realistic

values of molten state silicate viscosities. To bypass restrictions of the physical interpretation in this melt regime we employed the soft turbulence model by Kraichnan (1962) and Siggia (1994), and estimated the convective heat flux as

$$q = 0.089 \frac{k(T - T_{\text{surf}})}{D} Ra^{1/3}.$$

Using Equation 10 we derived an increased effective thermal conductivity

$$k_{\text{eff}} = \left(\frac{q}{0.089}\right)^{3/2} \frac{1}{(T - T_{\text{surf}})^2 \rho_{\text{eff}}} \left(\frac{\alpha g c_p}{\eta_{\text{num}}}\right)^{-1/2},$$

which approximates correct heat flux for a low viscosity magma ocean (Tackley et al., 2001; Hevey and Sanders, 2006; Golabek et al., 2011). For a more detailed discussion on model limitations due to this issue see Sect. 4.

2.4. Porosity

As already indicated in Sect. 1, the initial porous state of recently accreted planetesimals is thought to decrease due to cold isostatic pressing with pressure and thus depth into a configuration of closer packing (Henke et al., 2012), via

$$\phi(P) = 0.42 + 0.46 \cdot \left[\left(\frac{P}{P_0}\right)^{1.72} + 1\right]^{-1}, \quad (10)$$

with $P_0 = 0.13 \text{ bar}$, which effectively introduces an upper cut-off porosity for depths greater than $\sim 10^2 \text{ m}$, mostly dependent

PARAMETER	SYMBOL	VALUE RANGE	UNIT	LIST OF VALUES
Planetesimal radius	R_p	20–200	km	20, 50, 80, 110, 140, 170, 200
Instantaneous formation time	t_{form}	0.1–1.75	Myr	0.1, 0.5, 1.0, 1.1, 1.2, 1.3, 1.4, 1.5, 1.6, 1.7, 1.75
Initial porosity	ϕ_{init}	0.0–0.75		0.0, 0.1, 0.2, 0.25, 0.3, 0.4, 0.5, 0.75

Table 2: Distinct values of chosen parameter space.

on the size of the body. Furthermore, the porosity changes the density of the solid material

$$\rho_{\text{Si-por}}(P, T, \phi) = \rho_{\text{Si-sol}}(P, T) \cdot (1 - \phi), \quad (11)$$

and the effective thermal conductivity for porous material

$$k_{\text{eff,por}} = \begin{cases} k_1 = k \cdot e^{-\phi/\phi_0} & : \phi < 0.2, \\ k_3 = (k_1^4 + k_2^4)^{1/4} & : 0.2 \leq \phi \leq 0.4, \\ k_2 = k \cdot e^{a-\phi/\phi_1} & : \phi > 0.4, \end{cases} \quad (12)$$

with constants $a = -1.2$, $\phi_0 = 0.08$ and $\phi_1 = 0.167$, fitting lab experiments (Henke et al., 2012; Gail et al., 2015). Finally, the material compaction is sensitive to sintering effects via

$$\left| \frac{\partial \phi}{\partial t} \right| = A(1 - \phi) \frac{\sigma^{3/2}}{\mathfrak{R}^3} \cdot \exp \left[\frac{-E'_a}{RT} \right], \quad (13)$$

with the effective stress σ , the effective grain size \mathfrak{R} , the gas constant R and experimentally determined factors $A = 4 \cdot 10^{-5}$ and activation energy $E'_a = 85 \text{ kcal mol}^{-1}$ (Henke et al., 2012).

2.5. Initial conditions

The spherical planetesimals in our model box were supposed to be completely composed of silicates. Olivine outcrops pyroxene minerals in controlling deformation processes due to its mechanical weakness (Mackwell, 1991). Thus, we apply an olivine rheology (Ranalli, 1995) to be able to follow thermo-mechanical processes, i.e., melting and mixing due to internal heating. Each body was built up by several rheologically identical silicate layers, which could be followed by an internal tracking of the corresponding markers. This enabled us to distinguish different silicate layers and reconstruct their mixing history. Illustrative examples are given in Sect. 3.

As indicated before, the energy release during the accretion phase is only minor for the size of bodies we addressed here (Schubert et al., 1986). Therefore, we started from a constant temperature distribution all over the model grid in accordance with values in a typical protoplanetary disk $T_{\text{space}} = 290 \text{ K}$ (Ghosh and McSween, 1998).

The surrounding of the bodies was made up of a so-called sticky-air layer (Schmeling et al., 2008), with near zero density, constant temperature $T_{\text{SA}} = T_{\text{space}}$ and constant viscosity $\eta_{\text{SA}} = 10^{19} \text{ Pa}$. Such a layer allows for simulation of free surfaces and serves as infinite reservoir to absorb released heat from the planetesimal (Golabek et al., 2011; Cramer et al., 2012; Tkalec et al., 2013).

The numerical model boxes had physical dimensions of 500 km in each direction in 2D and 3D, represented by 501^2 grid

points in 2D, respectively 261^3 grid points in 3D, which results in physical resolutions of 1 km in 2D and $\sim 2 \text{ km}$ in 3D.

2.6. Parameter space

The goal of this work was to assess the combined effect of radiogenic heating by SLRs and initial porosity on the subsequent evolution of planetesimals. Hence, the parameter space was based on varying the planetesimal radius $R_p = 20\text{--}200 \text{ km}$, the instantaneous formation time $t_{\text{form}} = 0.1\text{--}1.75 \text{ Myr}$ after CAI formation and the initial porosity $\phi_{\text{init}} = 0.0\text{--}0.75$, in total a set of 616 2D simulations. A full list of all applied values is given in Table 2.

Due to the heavy computational cost of 3D simulations we first analyzed the 2D simulations, categorized them and then performed selected 3D simulations to verify the 2D results.

From our varied parameters, both R_p and t_{form} directly influenced the amount of SLRs present in the body. A list of all simulation runs with corresponding parameters and categories can be found for the 2D simulations in Table B.3 and for the 3D simulations in Table B.4.

3. Results

3.1. Thermo-mechanical evolution

In this section we analyze the thermo-mechanical outcome of the simulations. In Sect. 3.1.1 we focus on the temporal evolution of the material properties, i.e., solid or molten, and categorize the 2D results accordingly. Each category is then described and examples are given. In Sect. 3.1.2 we investigate the time-dependent maximum temperatures of the bodies and assess the influence of each of the varied parameters on it by constructing R_p , t_{form} and ϕ_{init} isolines. Also, we analyze the influence of ϕ_{init} on the temperature profile for fixed formation time and planetesimal size.

3.1.1. Material properties

Figure 1 illustrates the thermo-mechanical results of the material properties within each 2D simulation run. Each dot represents a single simulation and color indicates in which kind of regime we categorize the simulation. Each of these regimes is described below and an example, illustrating the state for ϕ , T and ρ at a certain time, is given. Illustrating video files for each of the described regimes below can be found in the supplementary material (see Appendix A).

2D thermomechanical regimes

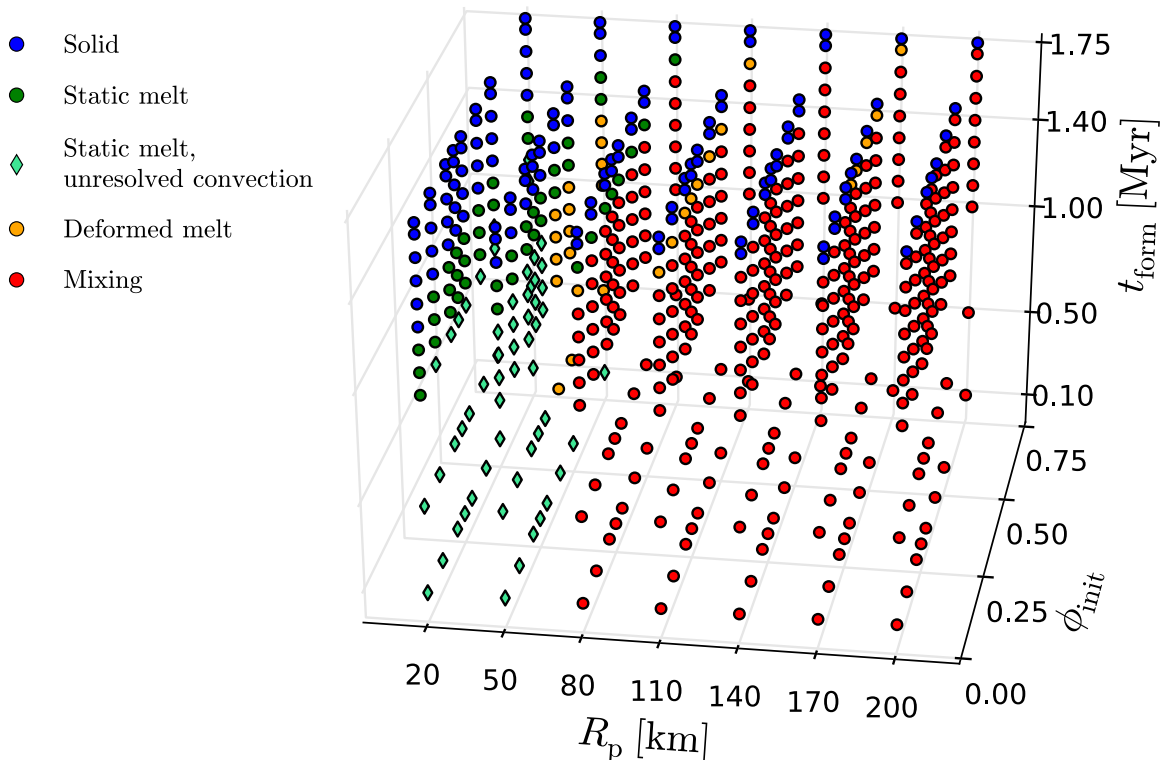


Figure 1: 3D parameter space covered by the two-dimensional simulation runs, each dot represents one simulation, with R_p in km, ϕ_{init} non-dimensional and t_{form} in Myr. The colors indicate which thermo-mechanical state was reached during the time evolution. *Blue*: all silicates were in solid form during all times (Fig. 2); *green*: the silicates in the planetesimal were partially or fully molten at some stage during the temporal evolution (Fig. 3), green simulations with diamonds indicate that the numerical restrictions in our model did not capture fluid motion due to extremely low viscosities, see Sect. 4 for an in-depth discussion of this issue; *orange*: the silicate layers were partially deformed, but the heating was not sufficient for convection (Fig. 4); *red*: convectational mixing occurs during the temporal evolution of the planetesimal (Fig. 5).

Solid regime. The blue rendered simulations in Fig. 1 build the class of *solid* models. These are models which lacked enough heat production by SLRs to experience any sign of transition from the solid silicate to a partially molten silicate state. An example of this kind is given in Fig. 2. The upper left image shows all simulation runs of this class. The composition plot illustrates the unperturbed layered structure of the silicates it is composed of. Because the body never experienced enough heat, no transition to a molten state occurred and therefore the layers resided with their original ordering. The temperature and density plots illustrate these parameters at the same time during the evolution. Since the body experienced some heat from SLRs it heated up and cooled down to the temperature of the surrounding T_{space} on the order of several tens of Myr. As shown in Fig. 2 these kinds of models can be found for all tested radii for $t_{form} \gtrsim 1.7$ Myr, i.e., when the initial amount of ^{26}Al has significantly reduced. Additionally, planetesimals with $R_p = 50$ km already belong to this class for earlier formation times $t_{form} \gtrsim 1.6$ Myr and for $t_{form} \gtrsim 1.3$ Myr for bodies with $R_p = 20$ km since they cooled more efficiently. Comparison of figures 1 and 2 for bodies with $R_p = 20$ km reveals the

influence of ϕ_{init} . For $t_{form} = 1.3$ Myr, the models were *solid* for $\phi_{init} \leq 0.3$ and *molten* for $\phi_{init} \geq 0.4$. Hence, the effects of initial porosity only affected this transitional stage for the smallest bodies in our parameter space.

Static melt regime. This class of simulations showed characteristics of phase transitions from solid to molten states, indicated with green circles and diamonds in Fig. 1. For the deviations between these we refer to the discussion of our model limitations in Sect. 4. An example of a *static melt* model is given in Fig. 3. In the composition Fig. we see molten silicate phases shown in red. As the material in the inner parts could not cool as efficiently as the outer parts higher temperatures occurred and thus silicates in this region tended to melt. Hence, the density in the outer shells was higher than in the inner parts. Simulations of this class were dominant for bodies with $R_p \leq 50$ km. For $R_p = 20$ km the boundary for the transition from solid to melt was $t_{form} \approx 1.3$ Myr, for $R_p = 50$ km it was $t_{form} \approx 1.6$ Myr. In bodies with $R_p = 80$ km this class could be found solely for $t_{form} = 1.6$ Myr, marking the boundary to the transition from solid models to more dynamic models displaying convection.

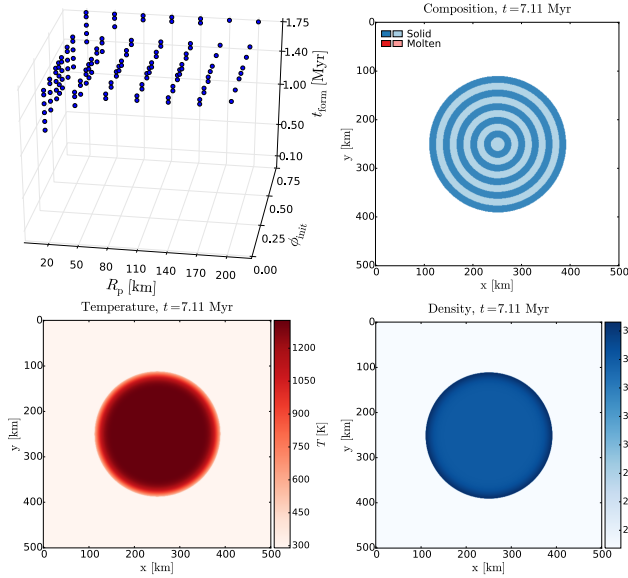


Figure 2: Example of a *solid* model, i.e., without any melting throughout the temporal evolution, with $R_p = 140$ km, $t_{\text{form}} = 1.7$ Myr, $\phi_{\text{init}} = 0.5$ at $t = 7.11$ Myr. The all-solid (rheologically identical) layers did not deform throughout the simulation.

Deformed melt regime. This class marked the transition from the *static melt* to the *mixing* regime in the three-dimensional parameter space. A *deformation* example is given in Fig. 4 for an evolutionary stage with molten silicate phases and deformed layers, which clearly deviated from the initial circular structure. This kind of models reached higher temperatures than their *static melt*-bearing counterparts. Due to the larger density contrast this led to the onset of mass segregation within the body. An interesting case is given for $R_p = 50$ km. These bodies were dominated by *deformation* for $\phi_{\text{init}} \geq 0.4$ and $t_{\text{form}} \lesssim 1.3$ Myr. This type is categorized differently as it indicates the restrictions of our model: if the viscosities fell below η_{num} , fluid motions could not always be correctly resolved, in spite of accurately modeling the heat flux. Again, for a more detailed discussion on this issue see Sect. 4.

Mixing regime. The class of *mixing* models was the most dynamic of all types. An example is given in Fig. 5, showing the onset of convection due to extreme heating conditions within the body due to high SLR abundances. In these cases the density contrast of inner and outer layers initiated and drove convective motion. The subsequent downwellings from the surface layers (cool and dense) to the inner parts (hot and buoyant) are reflected in the composition, temperature and density plots. We will discuss the time evolution of this in Sect. 3.1.2. Models of this kind were only found for bodies with $R_p \geq 80$ km. The formation time is less important than the radius, but showed significant effects by lowering the threshold t_{form} for smaller bodies, i.e., $R_p \leq 140$ km models did not *mix* anymore above $t_{\text{form}} \geq 1.6$ Myr, whereas $R_p \geq 170$ km models did. Even less influential for the qualitative evolution were changes in initial porosity, for which no significant variance was observed.

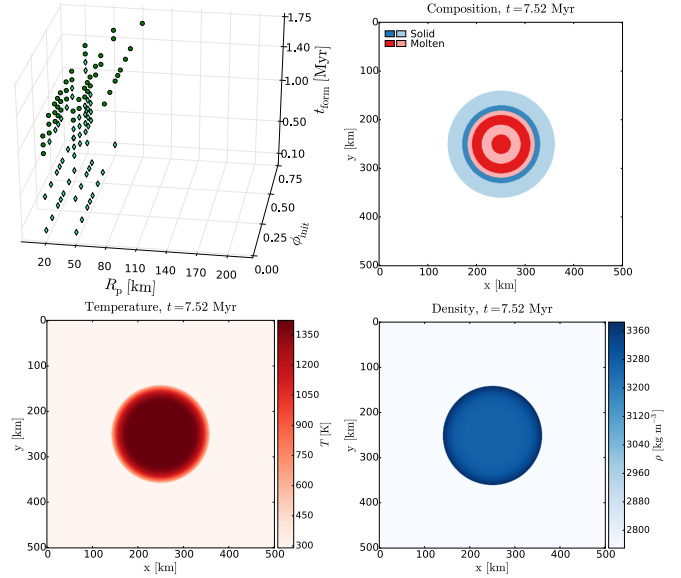


Figure 3: Example of a *static melt* model, with $R_p = 110$ km, $t_{\text{form}} = 1.6$ Myr, $\phi_{\text{init}} = 0.25$ at $t = 7.52$ Myr. The molten layers are differently shaded to be able to track the onset of convection (see Fig. 4). The inner parts were hotter and less dense than the upper layers and the temperatures were high enough to partially melt the silicates for a limited time period.

3.1.2. Heat balance

This section is devoted to an analysis of the energy reservoir in the bodies over time. To analyze the influence of each of the varied simulation parameters we construct isolines, fixing two of the three parameters (see figures 6 and 7). The models which are discussed here were among the simulations with the most extreme differences in peak temperature and are therefore best suited to show general trends in the data.

Influence of planetesimal radius R_p . Figure 6a shows the radius isolines for all R_p values for models with $t_{\text{form}} = 1.7$ Myr and $\phi_{\text{init}} = 0.25$. In general, smaller bodies cooled more efficiently than their larger counterparts, which were prone to reach higher temperatures. This resulted in lower viscosities for the latter and gave them more time to develop deformed structures or convection.

Influence of formation time t_{form} . Figure 6b shows the influence of the formation time on models with $R_p = 20$ km and $\phi_{\text{init}} = 0.4$. There are two interesting characteristics to note in this plot. Firstly, the bodies with $t_{\text{form}} = 0.1/0.5$ Myr showed a steep increase in temperature, compared to all other t_{form} isolines but reached a sudden turning point at $t \approx 7.2 \cdot 10^5$ Myr. These bodies incorporated more ^{26}Al due to its half-life time of $t_{1/2} \approx 7.2 \cdot 10^5$ Myr. When the temperatures increased, the material transitioned to molten states and viscosities $\eta \leq \eta_{\text{num}}$ occurred, the soft turbulence model set in and increased the heat flux, which permitted the body to cool at an elevated rate (see Sect. 4). Secondly, simulations with stronger heating sources and therefore higher peak temperatures showed steeper cooling

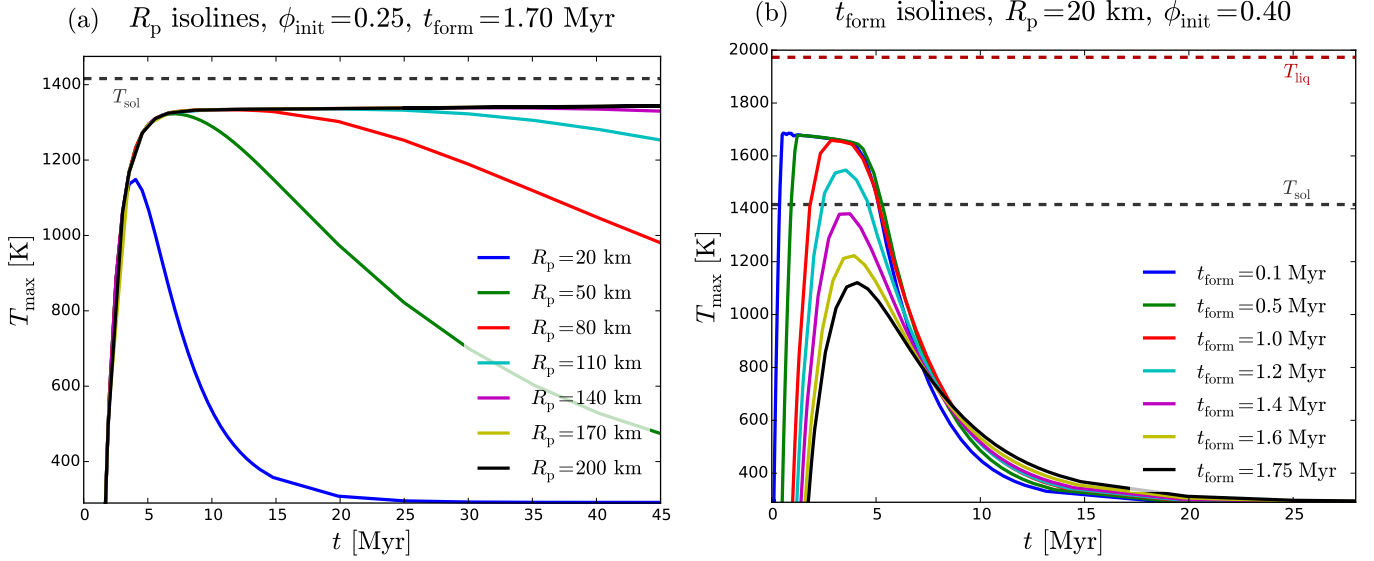


Figure 6: Peak temperature inside planetesimal versus time. T_{sol} and T_{liq} represent the solidus and liquidus temperatures, respectively. (a) Fixed ϕ_{init} , t_{form} and varying R_p . The cooling time scale is primarily dependent on the size of body. (b) Fixed R_p , ϕ_{init} and varying t_{form} . Only models with $t_{\text{form}} < 1.4$ Myr reached temperatures high enough for melting processes to occur. The $t_{\text{form}} = 0.1/0.5$ Myr models were affected by the soft turbulence model from Sect. 2.3, see Sect. 4 for a discussion of the effect.

curves than models with later formation time. In practice, the ordering of formation isolines is reverted at $t = 8$ Myr. This can be explained with the higher thermal conductivity of molten silicate states. The models with higher peak temperatures reached higher melt fractions than those with lower peak temperatures, and are therefore able to cool down more efficiently.

Influence of initial porosity ϕ_{init} . Figure 7 shows the contribution of initial porosity on peak temperature deviations in bodies with $R_p = 20$ km and $t_{\text{form}} = 1.75$ Myr. In general, higher porosity increases the voids within the granular material, effectively lowering the thermal conductivity. Therefore, models with higher initial porosity sustained their internal heat by SLRs over a longer time period. Fig. 7a shows an extreme case in the overall parameter range, where the maximum peak temperatures deviated by $\Delta T \approx 120$ K, not enough to achieve qualitative differences, as all peak temperatures were below the melting temperature for silicates.

To check for local variations of the temperature within specific planetesimals, we derive peak temperature profiles by assessing the maximum value from four points at the same distance from the planetesimal center. Therefore, the values in Fig. 7b represent the maximum temperatures at a certain depth, which does not necessarily imply the same average value for this depth for non-axisymmetric behavior. However, irrespective of a few specific cases these are nearly undistinguishable and certainly not in the range in which these differences affect the long-term thermo-mechanical evolution. Hence, we restrict our discussion to the maximum temperature case. The variations in peak temperature with depth were most importantly effecting small bodies, most remarkably $R_p = 20$ km in our parameter space. Therefore, Fig. 7b shows the porosity isolines

for the simulation with $R_p = 20$ km and $t_{\text{form}} = 1.75$ Myr at time $t = 4.61$ Myr. Going from the surface of the planetesimal to its center the temperature differences increased.

As displayed in both plots of Fig. 7, in such small planetesimals the peak temperatures were not enough for the onset of *melting*. Thus, the temperature deviations due to porosity changes did not result in qualitative differences between the displayed models. Since the peak temperature differences between porosity isolines decrease for all other parameter combinations the porosity did not have a significant effect on the thermo-mechanical evolution of the planetesimals.

3.2. Porous shells

Additional to the marginal effect of porosity changes on the peak temperature and the thermo-mechanical evolution, the majority of our models with initial porosity showed a porous shell feature. As illustrated for several models in Fig. 8, these structures were retained during the thermo-mechanical evolution and formed because of two effects. Firstly, compaction due to self-gravity by cold pressing (Equation 12) lowered the porosity within the body close to $\phi = 0.42$ and consequently increased the density contrast between the outermost layers and the layers deeper inside the body. Secondly, during the temporal evolution of the models the temperatures deep within the planetesimals were by far higher than those close to the surface. The temperatures within the body were high enough for sintering effects, which altered the porosity value according to Equation 15. Because both effects were unimportant closer to the surface, a large subset of the model retained a porous layer throughout their whole evolution. Only the models with the most extreme heating values were hot enough to sinter or melt even their outermost layers. Fig. 8 shows the combined effects of planetesi-

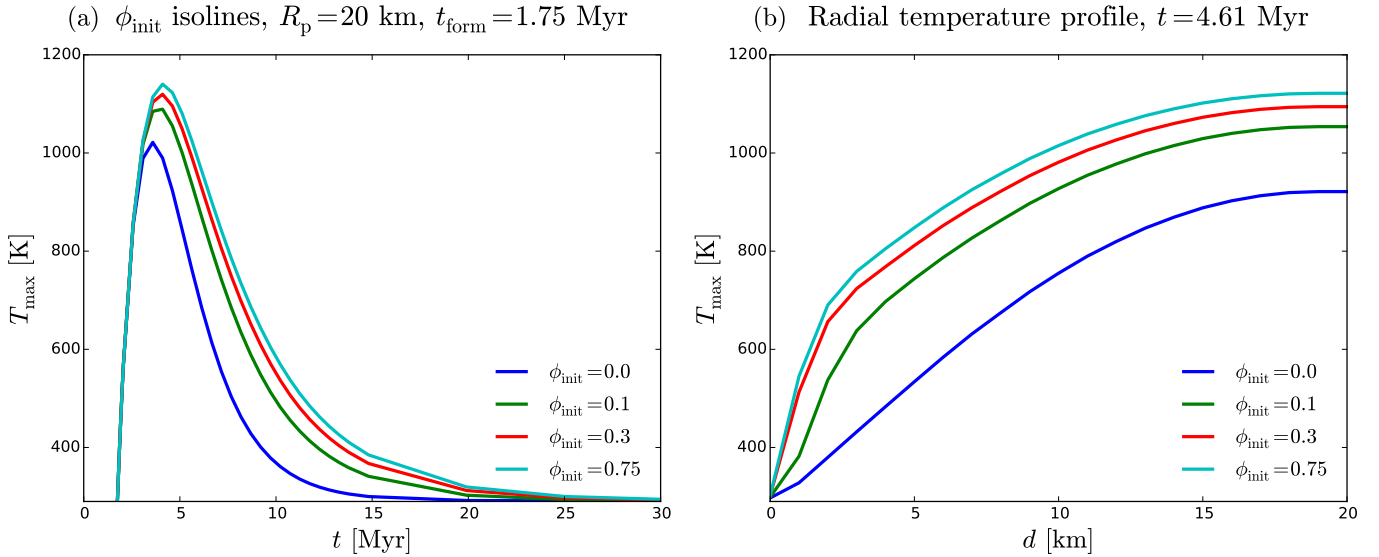


Figure 7: (a) Peak temperature inside planetesimal versus time with fixed R_p , t_{form} and varying ϕ_{init} . The models never reached temperatures high enough for melting processes to occur and the deviations in peak temperature were too small to inherit qualitative changes in the thermo-mechanical behavior of the simulations (compare Fig. 1.) (b) Peak temperature profiles inside planetesimal for time $t = 4.61$ Myr for the same parameters as plot (a). Deviations in peak temperature were more pronounced toward the center of the planetesimal.

mal size and formation time on the extent of the porous shells and the porosity change within the shell. Sintering limited the total thickness of the shell (d_{norm}) and compaction determined the increase in porosity toward the surface.

Figure 9 illustrates the distribution of bodies with and without porous shells. Most notably, the dominant parameter determining the preservation of a porous shell was the formation time: for $t_{\text{form}} \geq 1.0$ Myr all models developed such structures. Aside from the small effects of lithostatic pressure, the material distribution within the upper layers of the body did not depend on its size, since the weight on top of it was unaffected by the overall mass of the body. Therefore, these layers were only minimally affected by cold isostatic pressing. A minor effect regarding the size of the body was still observed, as models with $t_{\text{form}} = 0.5$ Myr and $R_p \leq 110$ km also developed a shell, while bodies with $R_p \geq 140$ km did not.

The distribution of the porous shell structures within the model set remained unaffected by initial porosity ϕ_{init} and was determined by R_p and t_{form} . Fig. 10 shows the thickness of the porous shell as a fraction of the size of the body R_p for different formation times t_{form} . The values represent an average over the results for all initial porosity values ϕ_{init} , as this parameter did not affect the final shell depths significantly. The fraction of the shell was larger for smaller bodies and for later formation times. Both vary the amount of heating sources within the body, as later formation times lowered the initial abundances of SLRs and smaller bodies cooled more efficiently and displayed lower temperatures in their interiors. Thus, sintering effects were less important.

3.3. 3D analogues

As described in Sect. 2.5 we additionally performed a set of 3D simulations for different parameter combinations to check for possible deviations from the 2D results. All 3D models are listed in Table B.4.

In principal, the selected 3D simulations confirmed the general trends we have found in two dimensions before. Smaller bodies with $R_p \leq 50$ km displayed *solid* or *static molten* type and developed no convection patterns, regardless of their formation time. Larger bodies were more likely to experience convective mixing, as illustrated in Fig. 11. Comparable to the 2D simulations the formation time was the dominant parameter for the thermo-mechanical evolution and the onset of melting processes: early formed bodies experienced stronger heating by SLRs. As expected from the 2D results we also found porous shells in the appropriate parameter ranges.

The 3D models, however, did not perfectly match the results from the 2D simulations, as can be seen for model number 624, with $R_p = 110$ km, $\phi_{\text{init}} = 0.25$ and $t_{\text{form}} = 1.7$ Myr, which evolved to a *static molten* state and did not retain a porous shell. Its 2D counterpart however was *solid* throughout its evolution and we found a shell at the end of its thermo-mechanical evolution. In general, as far as we can conclude from the restricted model set of 3D simulations, they seem to have experienced higher temperatures than their respective 2D analogues and thus the whole parameter space was shifted toward a higher fraction of *static molten*, *deformed molten* and *mixing* models. As already mentioned in the introduction, this result is expected and can be attributed to the lower surface-to-volume ratio of 3D models. Hence, planetesimals in 3D experienced a lower heat flux compared to their increased volume and abundance of

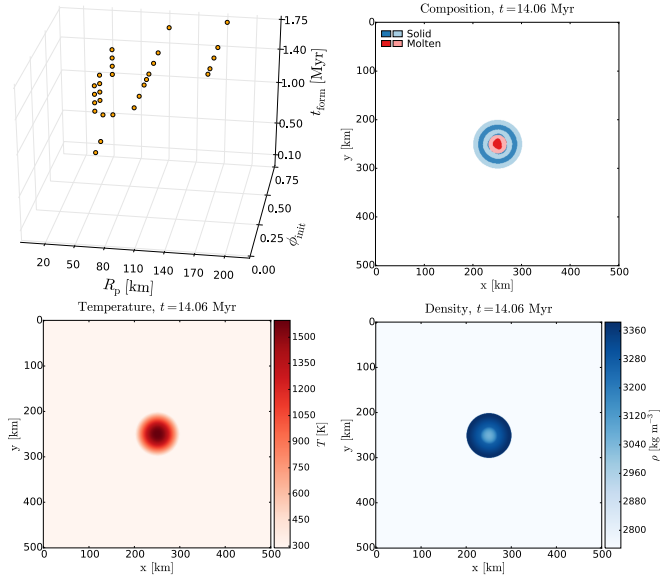


Figure 4: Example of a *deformation* model, with $R_p = 50$ km, $t_{\text{form}} = 1.0$ Myr, $\phi_{\text{init}} = 0.75$ at $t = 14.06$ Myr. The temperatures were high enough to initiate the onset of convection but could not sustain these temperatures long enough for mixing to occur.

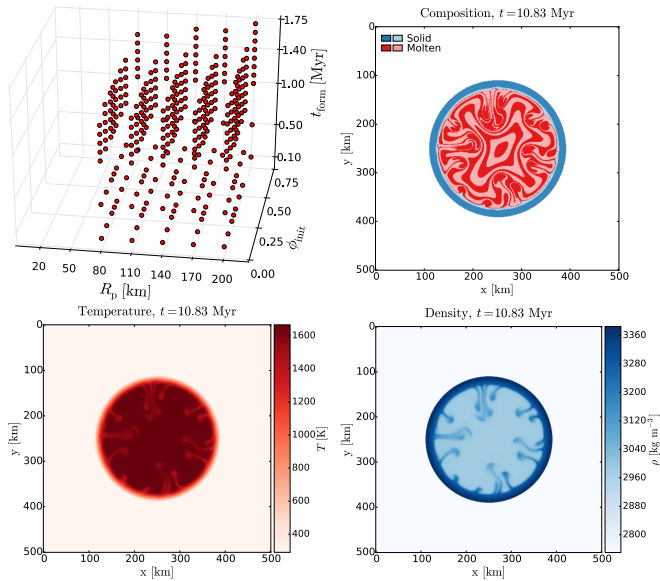


Figure 5: Example of a *mixing* model, with $R_p = 140$ km, $t_{\text{form}} = 0.5$ Myr, $\phi_{\text{init}} = 0.4$ at $t = 10.83$ Myr. The density contrast of inner and outer layers drove convection.

SLRs and therefore reached higher internal temperatures.

All in all, our 3D models were capable of reproducing the most important structures, compositional types and porosity features of the 2D models with slightly shifted regime boundaries and therefore verified the main conclusions we have drawn before.

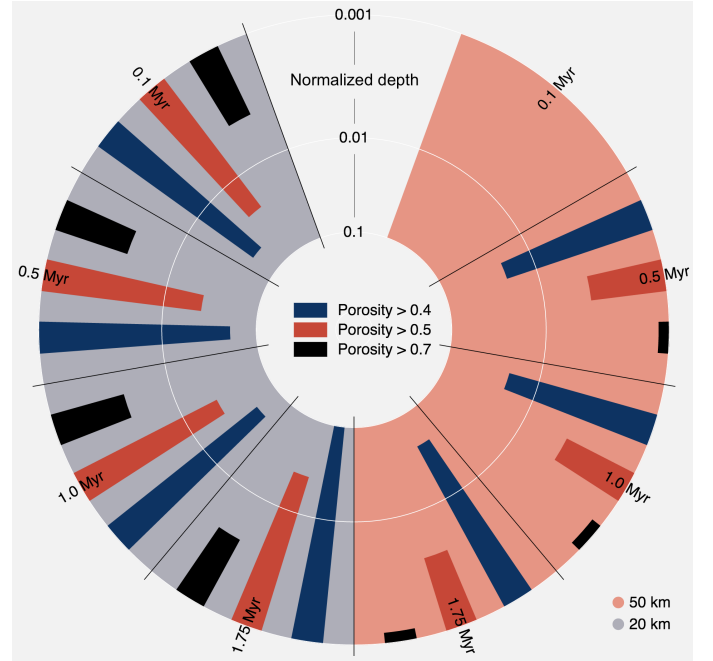


Figure 8: Remnant porous shells in evolved planetesimals with $R_p = 20$ km (gray background) or $R_p = 50$ km (red background), $\phi_{\text{init}} = 0.75$ and varying t_{form} . The tip of each dark blue bar represents the scaled thickness of the remnant porous shell at the end of the thermal evolution, with $\phi > 0.4$ (see Equation 12). As isostatic pressing effects decrease toward the surface, the red and black bars show depths above which the porosity was $\phi > 0.5$ or $\phi > 0.7$, respectively. The white circles represent normalized logarithmic depths within the planetesimal $d_{\text{norm}} = \log(d/R_p)$ from 0.001 to 0.1. As an example, the red bar for $R_p = 50$ km, $t_{\text{form}} = 0.5$ Myr shows that for $d_{\text{norm}} \lesssim 0.06$ the porosity was $\phi > 0.5$, increasing toward the surface.

4. Model limitations

The main caveat regarding the evolutionary channels from Sect. 3.1 is the lower cut-off viscosity η_{num} , whereas we expect that the real viscosity at melt fractions above 0.4 drops to values orders of magnitudes smaller than the applied lower cut-off viscosity (see Sect. 2.3 for examples). This especially happened for models with early formation times $t_{\text{form}} = 0.1/0.5$ Myr, i.e., within the first few half-life times of ^{26}Al . As mentioned before these low viscosities cannot be resolved numerically.

To estimate which of our numerical models would have experienced convection, that could not be resolved, we estimate the onset time of convection based on the approach of Howard (1964). Since internal heating was important in the models, we employ the Roberts-Rayleigh number (Roberts, 1967), which can be used to compute the boundary layer Roberts-Rayleigh number

$$Ra_\delta = \frac{\alpha g \rho_0 H_r \delta^5}{k \kappa \eta}, \quad (14)$$

with reference density ρ_0 , boundary layer thickness δ and thermal diffusivity κ . For the latter we use the characteristic dif-

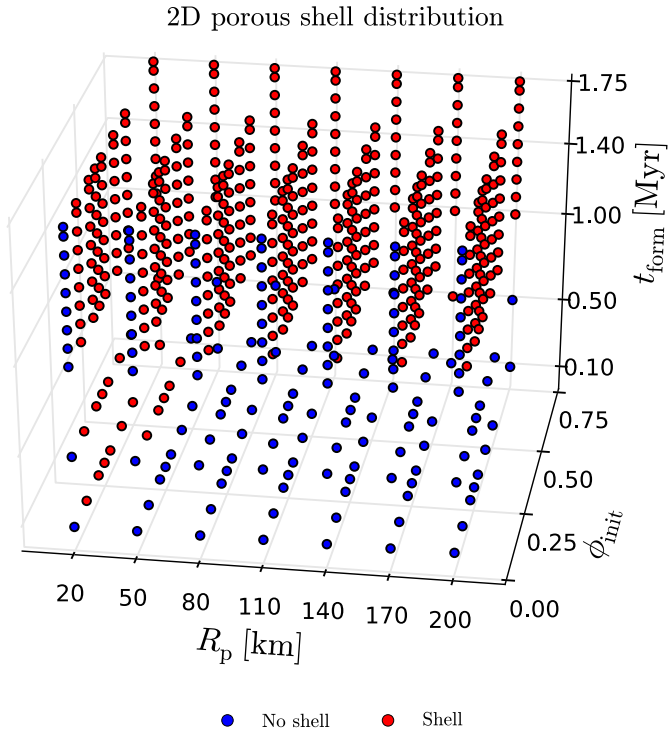


Figure 9: 3D parameter space showing the distribution of porous shells, with R_p in km, ϕ_{init} non-dimensional and t_{form} in Myr. The retainment of a porous shell depended dominantly on formation time t_{form} .

fusion lengthscale $(\kappa t)^{1/2}$ and assume that the viscosity of the partial melt decreases exponentially from 10^{17} Pa s at $\varphi = 0.4$ to 10^{-2} Pa s at $\varphi = 0.6$. Solving for t we obtain the relation

$$t_{\text{crit}} = \left(\frac{Ra_\delta \kappa \eta}{\alpha \rho_0 g H_r} \right)^{2/5} \kappa^{-3/5} \quad (15)$$

with $Ra_\delta \sim 30$ (Sotin and Labrosse, 1999). We use this relation to compare the time periods $\Delta t_{\eta \leq \eta_{\text{num}}}$, during which the viscosities are expected to drop below the numerical cut-off viscosity, with the analytical solution. Models with $t_{\text{crit}} \leq \Delta t_{\eta \leq \eta_{\text{num}}}$ are marked in Fig. 1 (diamonds, *static melt, unresolved convection*). These, together with the *deformed static* class, are models for which we could not properly resolve convection. This drawback, however, did not affect the purely thermal evolution of the models, which was correctly approximated by the soft turbulence approach (as shown in Tackley et al., 2001; Hevey and Sanders, 2006; Golabek et al., 2011) and therefore all other quantities were not affected. Models for which the analytic solution is consistent with pure melting and no convection ($t_{\text{crit}} > \Delta t_{\eta \leq \eta_{\text{num}}}$, circles in Fig. 1) are additionally listed in Tab. B.5 and are especially found for $t_{\text{form}} \approx 1.1 - 1.5$ Myr and $R_p = 20/50$ km.

Additionally, there are some minor aspects, which could shift the trends of our results, but not crucially change the general regimes. Firstly, all planetesimals were approximated as spherical bodies. Due to accretional processes in the early formation

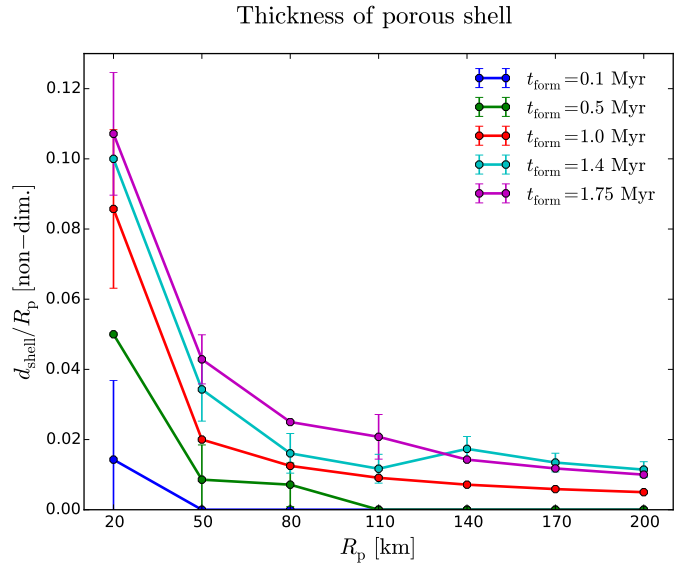


Figure 10: Fraction of porous shell versus planetesimal radius after all thermo-mechanical processes have ended. The values represent the arithmetic means over the results for all initial porosities ϕ_{init} , the errorbars showing the corresponding standard deviations. The shell fraction decreased with increasing size of the body and with earlier formation time.

phase, it is unlikely for planetesimals to be shaped perfectly symmetric. Irregular body structures would result in higher surface to volume ratios, hence enabling a faster cooling of the body (Davison et al., 2013).

Furthermore, as already discussed in Golabek et al. (2014), a more sophisticated approach for representing melt migration processes, cooling effects via ^{26}Al partitioning (Sahijpal et al., 2007) and iron-silicate-separation (Schubert et al., 1986) would incorporate a two-phase flow model, which was not featured here. Finally we did not consider the effect of melt composition on melt density, which would influence our *melting-mixing* boundary (Fu and Elkins-Tanton, 2014).

5. Discussion & implications

In Sect. 3 we have presented the results from our set of 2D and 3D computational models of the thermo-mechanical evolution of recently formed planetesimals with varied radius, instantaneous formation time and initial porosity to gain a better understanding of the processes in the early stages of terrestrial planet formation. We now discuss the key insights of our results.

Initial porosity of the bodies was only of minor importance for the model set we have run here. Although higher initial porosity tended to lower thermal conductivity and therefore favored higher internal temperatures, the thermo-mechanical evolution was only marginally affected.

As expected, radius of the body and formation time had a strong influence on the evolution of a planetesimal. With increasing radius and decreasing formation time the bodies ex-

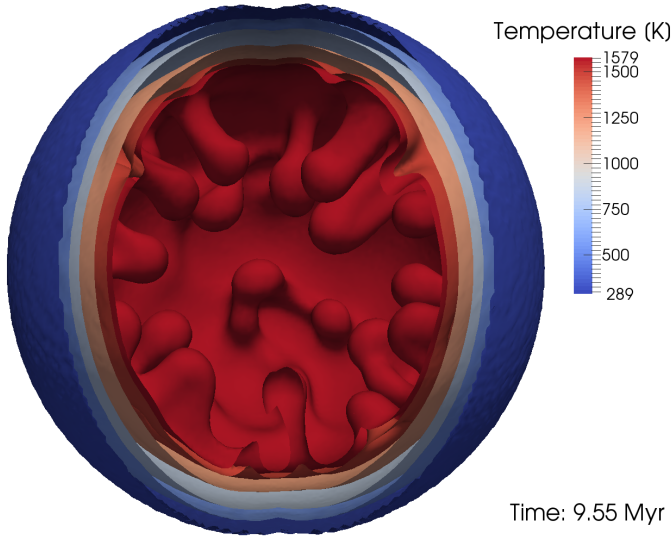


Figure 11: Density isocontours in a *mixing* 3D model, with $R_p = 110$ km, $\phi_{\text{init}} = 0.25$ and $t_{\text{form}} = 0.1$ Myr. The density increased from the inside (dark red, $\rho = 3100$ kg m $^{-3}$) to the outside (dark blue, $\rho = 3385.6$ kg m $^{-3}$). Therefore, the model experienced buoyancy driven mass movement.

perienced more heating by SLRs, which resulted in higher peak temperatures and steeper heating curves. Planetesimals displaying *mixing* can be expected to have experienced iron-silicate separation. The fraction of bodies prone to significant internal silicate melting was consistent with previous work on the thermal histories of planetesimals (Sanders and Taylor, 2005).

With decreasing radius of the body the technical assessment of the numerical model became more important, as a thermo-mechanical regime with partially molten, but non-convectational interior was observed (static melt class in Fig. 1). In this regime with $\varphi \lesssim 0.4$ we expect the Stokes velocity $v_{\text{Stokes}} \sim g/\eta$ for iron droplets to be small, such that the time scale for differentiation is high. These melt-bearing but undifferentiated planetesimals are a potentially important link for impact splash models of chondrule formation (see, e.g., Sanders and Taylor, 2005; Sanders and Scott, 2012; Dullemond et al., 2014). For a more stringent analysis of the importance of these models and corresponding parameter ranges we will further evaluate this connection in future work.

A subset of our models evolved to a state with highly porous outer layers, which altered the cooling history of the planetesimal. These shells occupied a larger fraction of the planetesimal radius with later formation time and smaller radius of the body. Hence, smaller and later formed objects were the most powdery bodies, which can have implications on their dynamical behavior during impact processes, as investigated by Jutzi et al. (2008, 2009). The larger planetesimals in our dataset can either be subject to catastrophic impact events with similar-sized bodies or subject to impacts by smaller bodies. For both cases the state of the material is important for the interaction with the encountered body. All in all these effects tend to influence the

dynamical history of the accretion phase of terrestrial planets and cannot be neglected for investigations of collisional growth. Additionally, the thickness of the shells could be used to relate the structure of pristine bodies in the Solar System, which did not experience catastrophic impact events after their rapid formation, to their formation time.

Many of our models reached elevated temperatures, potentially high enough to outgas existing volatile elements. When these models reached a specific boundary the resulting bodies might end up as dry bodies, unable to deliver volatile elements to the forming planets via impacts. Thus, future studies will investigate the effect of SLR heating and initial porosity on the outgassing of volatiles in small bodies and therefore might have implications for the habitability of planetary systems, when related to the delivery to accreting terrestrial planets (e.g., Elser et al., 2012; Ciesla et al., 2015).

The more moderate models still showed temperatures high enough for hydration and metamorphic transformation processes, potentially creating serpentinites via an exothermic reaction. As discussed in Abramov and Mojzsis (2011) such reactions can provide energy for non-volcanic hydrothermal activity. Within certain depths of onion shell structured planetesimals, which are in accordance with our models and previous work (Weiss and Elkins-Tanton, 2013, and references therein), the energy output might be in the right regime for the synthesis of primitive organic compounds, such as basic amino acids (Cobb and Pudritz, 2014). Their synthesis is dependent on the ammonia and water content of the corresponding planetesimal and can also change with radial distance to the central star (Cobb et al., 2015). Therefore, future studies can be directed to couple interior evolution to exterior formation conditions, i.e., the region in the protoplanetary disk and the appropriate formation time for various size classes, to gain a better understanding of the geological environment of early biological processes in our Solar System.

6. Conclusions

The initial state of planetesimals in the early Solar System crucially affected their thermo-mechanical evolution, which yields implications for terrestrial planet formation theories. We have conducted numerous 2D and 3D finite-difference fluid dynamics simulations of planetesimals with varying radius, formation time and initial porosity. From these we have determined the parameter space for various thermo-mechanical regimes and the influence of initial porosity. Our conclusions are the following.

- Typically, planetesimals with large size, early formation time and high initial porosity tended to develop convection. Small radii, late formation times and low porosities led to bodies which did not experience silicate melting.
- A third thermo-mechanical regime with largely molten bodies without convectational mixing existed for an intermediate parameter range with a trend toward small bodies and formation times $t_{\text{form}} \approx 1.1\text{--}1.5$ Myr after CAI formation.

- The effects of initial porosity were by far outweighed by those of planetesimal size and formation time, scarcely affecting the qualitative evolution of a planetesimal.
- A majority of models retained a shell of highly porous material in their outer layers, which was not affected by melting and sintering processes inside the bodies. The depth of these shells increased with later formation times and decreased planetesimal size.

No.	R_p	ϕ_{init}	t_{form}	GRID	SHELL	THERMOM. REGIME	UNR. CONV.
001	20	0	0.1	501 ²	No	Static melt	Yes
002	20	0	0.5	501 ²	No	Static melt	Yes

With our models we were able to constrain stringent parameter ranges for the major thermo-mechanical regimes and to show that porosity is not a primary factor for the evolution of planetesimals. Future investigations will link these results to specific aspects of terrestrial planet formation, like volatile degassing and chondrule formation. Moreover, connecting these results with SLR enrichment mechanisms in stellar clusters (e.g., Parker et al., 2014; Parker and Dale, 2016), and thus probably strongly varying abundances of SLRs, would be beneficial for a comprehensive theory of planetary assembly and habitability on interstellar or galactic scales.

Acknowledgements

We thank the referee Stephen J. Mojzsis for a thorough and constructive review, which considerably helped to improve the manuscript. We thank the NCCR PlanetS and the PlanetZ platforms for an inspiring and collaborative scientific environment and Richard J. Parker and Cornelis P. Dullemond for stimulating discussions. TL was supported by ETH Research Grant ETH-17 13-1. The numerical simulations in this work were performed on the BRUTUS and EULER computing clusters of ETH Zürich. The models were analyzed using the open source software environments MATPLOTLIB¹ (Hunter, 2007), BOKEH² and PARAVIEW³ (Ahrens et al., 2005).

Appendix A. Supplementary material

Supplementary data associated with this article can be found, in the online version, at <http://dx.doi.org/10.1016/j.icarus.2016.03.004>.

Appendix B. List of simulation runs

Table B.3: List of all 2D simulations with radius R_p (km), formation time t_{form} (Myr) and initial porosity ϕ_{init} (non-dim.). GRID specifies the number of nodes in the finite-difference grid, SHELL indicates whether the corresponding model retained a porous shell after its thermo-mechanical evolution, THERMOM. REGIME indicates the evolutionary channel of the model and UNR. CONV. states whether the model resolved the internal fluid motion.

¹<http://matplotlib.org>

²<http://bokeh.pydata.org>

³<http://www.paraview.org>

No.	R_p	ϕ_{init}	t_{form}	GRID	SHELL	THERMOM. REGIME	UNR. CONV.	No.	R_p	ϕ_{init}	t_{form}	GRID	SHELL	THERMOM. REGIME	UNR. CONV.
003	20	0	1	501 ²	No	Static melt	No	066	20	0.4	1.75	501 ²	Yes	Solid	No
004	20	0	1.1	501 ²	No	Static melt	No	067	20	0.5	0.1	501 ²	Yes	Static melt	Yes
005	20	0	1.2	501 ²	No	Static melt	No	068	20	0.5	0.5	501 ²	Yes	Static melt	Yes
006	20	0	1.3	501 ²	No	Solid	No	069	20	0.5	1	501 ²	Yes	Static melt	Yes
007	20	0	1.4	501 ²	No	Solid	No	070	20	0.5	1.1	501 ²	Yes	Static melt	Yes
008	20	0	1.5	501 ²	No	Solid	No	071	20	0.5	1.2	501 ²	Yes	Static melt	No
009	20	0	1.6	501 ²	No	Solid	No	072	20	0.5	1.3	501 ²	Yes	Static melt	No
010	20	0	1.7	501 ²	No	Solid	No	073	20	0.5	1.4	501 ²	Yes	Solid	No
011	20	0	1.75	501 ²	No	Solid	No	074	20	0.5	1.5	501 ²	Yes	Solid	No
012	20	0.1	0.1	501 ²	Yes	Static melt	Yes	075	20	0.5	1.6	501 ²	Yes	Solid	No
013	20	0.1	0.5	501 ²	Yes	Static melt	Yes	076	20	0.5	1.7	501 ²	Yes	Solid	No
014	20	0.1	1	501 ²	Yes	Static melt	Yes	077	20	0.5	1.75	501 ²	Yes	Solid	No
015	20	0.1	1.1	501 ²	Yes	Static melt	No	078	20	0.75	0.1	501 ²	Yes	Static melt	Yes
016	20	0.1	1.2	501 ²	Yes	Static melt	No	079	20	0.75	0.5	501 ²	Yes	Static melt	Yes
017	20	0.1	1.3	501 ²	Yes	Static melt	No	080	20	0.75	1	501 ²	Yes	Static melt	Yes
018	20	0.1	1.4	501 ²	Yes	Solid	No	081	20	0.75	1.1	501 ²	Yes	Static melt	Yes
019	20	0.1	1.5	501 ²	Yes	Solid	No	082	20	0.75	1.2	501 ²	Yes	Static melt	No
020	20	0.1	1.6	501 ²	Yes	Solid	No	083	20	0.75	1.3	501 ²	Yes	Static melt	No
021	20	0.1	1.7	501 ²	Yes	Solid	No	084	20	0.75	1.4	501 ²	Yes	Solid	No
022	20	0.1	1.75	501 ²	Yes	Solid	No	085	20	0.75	1.5	501 ²	Yes	Solid	No
023	20	0.2	0.1	501 ²	Yes	Static melt	Yes	086	20	0.75	1.6	501 ²	Yes	Solid	No
024	20	0.2	0.5	501 ²	Yes	Static melt	Yes	087	20	0.75	1.7	501 ²	Yes	Solid	No
025	20	0.2	1	501 ²	Yes	Static melt	Yes	088	20	0.75	1.75	501 ²	Yes	Solid	No
026	20	0.2	1.1	501 ²	Yes	Static melt	No	089	50	0	0.1	501 ²	No	Static melt	Yes
027	20	0.2	1.2	501 ²	Yes	Static melt	No	090	50	0	0.5	501 ²	No	Static melt	Yes
028	20	0.2	1.3	501 ²	Yes	Static melt	No	091	50	0	1	501 ²	No	Static melt	Yes
029	20	0.2	1.4	501 ²	Yes	Solid	No	092	50	0	1.1	501 ²	No	Static melt	Yes
030	20	0.2	1.5	501 ²	Yes	Solid	No	093	50	0	1.2	501 ²	No	Static melt	Yes
031	20	0.2	1.6	501 ²	Yes	Solid	No	094	50	0	1.3	501 ²	No	Static melt	Yes
032	20	0.2	1.7	501 ²	Yes	Solid	No	095	50	0	1.4	501 ²	No	Static melt	No
033	20	0.2	1.75	501 ²	Yes	Solid	No	096	50	0	1.5	501 ²	No	Static melt	No
034	20	0.25	0.1	501 ²	Yes	Static melt	Yes	097	50	0	1.6	501 ²	No	Solid	No
035	20	0.25	0.5	501 ²	Yes	Static melt	Yes	098	50	0	1.7	501 ²	No	Solid	No
036	20	0.25	1	501 ²	Yes	Static melt	Yes	099	50	0	1.75	501 ²	No	Solid	No
037	20	0.25	1.1	501 ²	Yes	Static melt	No	100	50	0.1	0.1	501 ²	No	Static melt	Yes
038	20	0.25	1.2	501 ²	Yes	Static melt	No	101	50	0.1	0.5	501 ²	Yes	Static melt	Yes
039	20	0.25	1.3	501 ²	Yes	Static melt	No	102	50	0.1	1	501 ²	Yes	Static melt	Yes
040	20	0.25	1.4	501 ²	Yes	Solid	No	103	50	0.1	1.1	501 ²	Yes	Static melt	Yes
041	20	0.25	1.5	501 ²	Yes	Solid	No	104	50	0.1	1.2	501 ²	Yes	Static melt	Yes
042	20	0.25	1.6	501 ²	Yes	Solid	No	105	50	0.1	1.3	501 ²	Yes	Static melt	Yes
043	20	0.25	1.7	501 ²	Yes	Solid	No	106	50	0.1	1.4	501 ²	Yes	Static melt	No
044	20	0.25	1.75	501 ²	Yes	Solid	No	107	50	0.1	1.5	501 ²	Yes	Static melt	No
045	20	0.3	0.1	501 ²	Yes	Static melt	Yes	108	50	0.1	1.6	501 ²	Yes	Solid	No
046	20	0.3	0.5	501 ²	Yes	Static melt	Yes	109	50	0.1	1.7	501 ²	Yes	Solid	No
047	20	0.3	1	501 ²	Yes	Static melt	Yes	110	50	0.1	1.75	501 ²	Yes	Solid	No
048	20	0.3	1.1	501 ²	Yes	Static melt	No	111	50	0.2	0.1	501 ²	No	Static melt	Yes
049	20	0.3	1.2	501 ²	Yes	Static melt	No	112	50	0.2	0.5	501 ²	Yes	Static melt	Yes
050	20	0.3	1.3	501 ²	Yes	Static melt	No	113	50	0.2	1	501 ²	Yes	Static melt	Yes
051	20	0.3	1.4	501 ²	Yes	Solid	No	114	50	0.2	1.1	501 ²	Yes	Static melt	Yes
052	20	0.3	1.5	501 ²	Yes	Solid	No	115	50	0.2	1.2	501 ²	Yes	Static melt	Yes
053	20	0.3	1.6	501 ²	Yes	Solid	No	116	50	0.2	1.3	501 ²	Yes	Static melt	Yes
054	20	0.3	1.7	501 ²	Yes	Solid	No	117	50	0.2	1.4	501 ²	Yes	Static melt	No
055	20	0.3	1.75	501 ²	Yes	Solid	No	118	50	0.2	1.5	501 ²	Yes	Static melt	No
056	20	0.4	0.1	501 ²	Yes	Static melt	Yes	119	50	0.2	1.6	501 ²	Yes	Solid	No
057	20	0.4	0.5	501 ²	Yes	Static melt	Yes	120	50	0.2	1.7	501 ²	Yes	Solid	No
058	20	0.4	1	501 ²	Yes	Static melt	Yes	121	50	0.2	1.75	501 ²	Yes	Solid	No
059	20	0.4	1.1	501 ²	Yes	Static melt	No	122	50	0.25	0.1	501 ²	No	Static melt	Yes
060	20	0.4	1.2	501 ²	Yes	Static melt	No	123	50	0.25	0.5	501 ²	Yes	Static melt	Yes
061	20	0.4	1.3	501 ²	Yes	Static melt	No	124	50	0.25	1	501 ²	Yes	Static melt	Yes
062	20	0.4	1.4	501 ²	Yes	Solid	No	125	50	0.25	1.1	501 ²	Yes	Static melt	Yes
063	20	0.4	1.5	501 ²	Yes	Solid	No	126	50	0.25	1.2	501 ²	Yes	Static melt	Yes
064	20	0.4	1.6	501 ²	Yes	Solid	No	127	50	0.25	1.3	501 ²	Yes	Static melt	Yes
065	20	0.4	1.7	501 ²	Yes	Solid	No	128	50	0.25	1.4	501 ²	Yes	Static melt	No

No.	R_p	ϕ_{init}	t_{form}	GRID	SHELL	THERMOM. REGIME	UNR. CONV.	No.	R_p	ϕ_{init}	t_{form}	GRID	SHELL	THERMOM. REGIME	UNR. CONV.
129	50	0.25	1.5	501 ²	Yes	Static melt	No	192	80	0.1	1.2	501 ²	Yes	Mixing	Yes
130	50	0.25	1.6	501 ²	Yes	Solid	No	193	80	0.1	1.3	501 ²	Yes	Mixing	Yes
131	50	0.25	1.7	501 ²	Yes	Solid	No	194	80	0.1	1.4	501 ²	Yes	Mixing	No
132	50	0.25	1.75	501 ²	Yes	Solid	No	195	80	0.1	1.5	501 ²	Yes	Mixing	No
133	50	0.3	0.1	501 ²	No	Static melt	Yes	196	80	0.1	1.6	501 ²	Yes	Static melt	No
134	50	0.3	0.5	501 ²	Yes	Static melt	Yes	197	80	0.1	1.7	501 ²	Yes	Solid	No
135	50	0.3	1	501 ²	Yes	Static melt	Yes	198	80	0.1	1.75	501 ²	Yes	Solid	No
136	50	0.3	1.1	501 ²	Yes	Static melt	Yes	199	80	0.2	0.1	501 ²	No	Mixing	Yes
137	50	0.3	1.2	501 ²	Yes	Static melt	Yes	200	80	0.2	0.5	501 ²	No	Mixing	Yes
138	50	0.3	1.3	501 ²	Yes	Static melt	Yes	201	80	0.2	1	501 ²	Yes	Mixing	Yes
139	50	0.3	1.4	501 ²	Yes	Static melt	No	202	80	0.2	1.1	501 ²	Yes	Mixing	Yes
140	50	0.3	1.5	501 ²	Yes	Static melt	No	203	80	0.2	1.2	501 ²	Yes	Mixing	Yes
141	50	0.3	1.6	501 ²	Yes	Solid	No	204	80	0.2	1.3	501 ²	Yes	Mixing	Yes
142	50	0.3	1.7	501 ²	Yes	Solid	No	205	80	0.2	1.4	501 ²	Yes	Mixing	No
143	50	0.3	1.75	501 ²	Yes	Solid	No	206	80	0.2	1.5	501 ²	Yes	Mixing	No
144	50	0.4	0.1	501 ²	No	Static melt	Yes	207	80	0.2	1.6	501 ²	Yes	Static melt	No
145	50	0.4	0.5	501 ²	Yes	Def. melt	Yes	208	80	0.2	1.7	501 ²	Yes	Solid	No
146	50	0.4	1	501 ²	Yes	Def. melt	Yes	209	80	0.2	1.75	501 ²	Yes	Solid	No
147	50	0.4	1.1	501 ²	Yes	Def. melt	Yes	210	80	0.25	0.1	501 ²	No	Mixing	Yes
148	50	0.4	1.2	501 ²	Yes	Def. melt	Yes	211	80	0.25	0.5	501 ²	No	Mixing	Yes
149	50	0.4	1.3	501 ²	Yes	Def. melt	Yes	212	80	0.25	1	501 ²	Yes	Mixing	Yes
150	50	0.4	1.4	501 ²	Yes	Static melt	No	213	80	0.25	1.1	501 ²	Yes	Mixing	Yes
151	50	0.4	1.5	501 ²	Yes	Static melt	No	214	80	0.25	1.2	501 ²	Yes	Mixing	Yes
152	50	0.4	1.6	501 ²	Yes	Solid	No	215	80	0.25	1.3	501 ²	Yes	Mixing	Yes
153	50	0.4	1.7	501 ²	Yes	Solid	No	216	80	0.25	1.4	501 ²	Yes	Mixing	No
154	50	0.4	1.75	501 ²	Yes	Solid	No	217	80	0.25	1.5	501 ²	Yes	Mixing	No
155	50	0.5	0.1	501 ²	No	Static melt	Yes	218	80	0.25	1.6	501 ²	Yes	Static melt	No
156	50	0.5	0.5	501 ²	No	Def. melt	Yes	219	80	0.25	1.7	501 ²	Yes	Solid	No
157	50	0.5	1	501 ²	Yes	Def. melt	Yes	220	80	0.25	1.75	501 ²	Yes	Solid	No
158	50	0.5	1.1	501 ²	Yes	Def. melt	Yes	221	80	0.3	0.1	501 ²	No	Mixing	Yes
159	50	0.5	1.2	501 ²	Yes	Def. melt	Yes	222	80	0.3	0.5	501 ²	No	Mixing	Yes
160	50	0.5	1.3	501 ²	Yes	Def. melt	Yes	223	80	0.3	1	501 ²	Yes	Mixing	Yes
161	50	0.5	1.4	501 ²	Yes	Static melt	No	224	80	0.3	1.1	501 ²	Yes	Mixing	Yes
162	50	0.5	1.5	501 ²	Yes	Static melt	No	225	80	0.3	1.2	501 ²	Yes	Mixing	Yes
163	50	0.5	1.6	501 ²	Yes	Solid	No	226	80	0.3	1.3	501 ²	Yes	Mixing	Yes
164	50	0.5	1.7	501 ²	Yes	Solid	No	227	80	0.3	1.4	501 ²	Yes	Mixing	No
165	50	0.5	1.75	501 ²	Yes	Solid	No	228	80	0.3	1.5	501 ²	Yes	Mixing	No
166	50	0.75	0.1	501 ²	No	Static melt	Yes	229	80	0.3	1.6	501 ²	Yes	Static melt	No
167	50	0.75	0.5	501 ²	No	Def. melt	Yes	230	80	0.3	1.7	501 ²	Yes	Solid	No
168	50	0.75	1	501 ²	Yes	Def. melt	Yes	231	80	0.3	1.75	501 ²	Yes	Solid	No
169	50	0.75	1.1	501 ²	Yes	Def. melt	Yes	232	80	0.4	0.1	501 ²	No	Mixing	Yes
170	50	0.75	1.2	501 ²	Yes	Def. melt	Yes	233	80	0.4	0.5	501 ²	No	Mixing	Yes
171	50	0.75	1.3	501 ²	Yes	Def. melt	Yes	234	80	0.4	1	501 ²	Yes	Mixing	Yes
172	50	0.75	1.4	501 ²	Yes	Static melt	No	235	80	0.4	1.1	501 ²	Yes	Mixing	Yes
173	50	0.75	1.5	501 ²	Yes	Static melt	No	236	80	0.4	1.2	501 ²	Yes	Mixing	Yes
174	50	0.75	1.6	501 ²	Yes	Solid	No	237	80	0.4	1.3	501 ²	Yes	Mixing	Yes
175	50	0.75	1.7	501 ²	Yes	Solid	No	238	80	0.4	1.4	501 ²	Yes	Mixing	No
176	50	0.75	1.75	501 ²	Yes	Solid	No	239	80	0.4	1.5	501 ²	Yes	Mixing	No
177	80	0	0.1	501 ²	No	Mixing	Yes	240	80	0.4	1.6	501 ²	Yes	Static melt	No
178	80	0	0.5	501 ²	No	Mixing	Yes	241	80	0.4	1.7	501 ²	Yes	Solid	No
179	80	0	1	501 ²	No	Mixing	Yes	242	80	0.4	1.75	501 ²	Yes	Solid	No
180	80	0	1.1	501 ²	No	Mixing	Yes	243	80	0.5	0.1	501 ²	No	Mixing	Yes
181	80	0	1.2	501 ²	No	Mixing	Yes	244	80	0.5	0.5	501 ²	No	Mixing	Yes
182	80	0	1.3	501 ²	No	Mixing	Yes	245	80	0.5	1	501 ²	Yes	Mixing	Yes
183	80	0	1.4	501 ²	No	Mixing	No	246	80	0.5	1.1	501 ²	Yes	Mixing	Yes
184	80	0	1.5	501 ²	No	Def. melt	No	247	80	0.5	1.2	501 ²	Yes	Mixing	Yes
185	80	0	1.6	501 ²	No	Static melt	No	248	80	0.5	1.3	501 ²	Yes	Mixing	Yes
186	80	0	1.7	501 ²	No	Solid	No	249	80	0.5	1.4	501 ²	Yes	Mixing	No
187	80	0	1.75	501 ²	No	Solid	No	250	80	0.5	1.5	501 ²	Yes	Mixing	No
188	80	0.1	0.1	501 ²	No	Mixing	Yes	251	80	0.5	1.6	501 ²	Yes	Static melt	No
189	80	0.1	0.5	501 ²	No	Mixing	Yes	252	80	0.5	1.7	501 ²	Yes	Solid	No
190	80	0.1	1	501 ²	Yes	Mixing	Yes	253	80	0.5	1.75	501 ²	Yes	Solid	No
191	80	0.1	1.1	501 ²	Yes	Mixing	Yes	254	80	0.75	0.1	501 ²	No	Mixing	Yes

No.	R_p	ϕ_{init}	t_{form}	GRID	SHELL	THERMOM. REGIME	UNR. CONV.	No.	R_p	ϕ_{init}	t_{form}	GRID	SHELL	THERMOM. REGIME	UNR. CONV.
255	80	0.75	0.5	501 ²	No	Mixing	Yes	318	110	0.3	1.7	501 ²	Yes	Solid	No
256	80	0.75	1	501 ²	Yes	Mixing	Yes	319	110	0.3	1.75	501 ²	Yes	Solid	No
257	80	0.75	1.1	501 ²	Yes	Mixing	Yes	320	110	0.4	0.1	501 ²	No	Mixing	Yes
258	80	0.75	1.2	501 ²	Yes	Mixing	Yes	321	110	0.4	0.5	501 ²	No	Mixing	Yes
259	80	0.75	1.3	501 ²	Yes	Mixing	Yes	322	110	0.4	1	501 ²	Yes	Mixing	Yes
260	80	0.75	1.4	501 ²	Yes	Mixing	No	323	110	0.4	1.1	501 ²	Yes	Mixing	Yes
261	80	0.75	1.5	501 ²	Yes	Mixing	No	324	110	0.4	1.2	501 ²	Yes	Mixing	Yes
262	80	0.75	1.6	501 ²	Yes	Static melt	No	325	110	0.4	1.3	501 ²	Yes	Mixing	Yes
263	80	0.75	1.7	501 ²	Yes	Solid	No	326	110	0.4	1.4	501 ²	Yes	Mixing	No
264	80	0.75	1.75	501 ²	Yes	Solid	No	327	110	0.4	1.5	501 ²	Yes	Mixing	No
265	110	0	0.1	501 ²	No	Mixing	Yes	328	110	0.4	1.6	501 ²	Yes	Def. melt	No
266	110	0	0.5	501 ²	No	Mixing	Yes	329	110	0.4	1.7	501 ²	Yes	Solid	No
267	110	0	1	501 ²	No	Mixing	Yes	330	110	0.4	1.75	501 ²	Yes	Solid	No
268	110	0	1.1	501 ²	No	Mixing	Yes	331	110	0.5	0.1	501 ²	No	Mixing	Yes
269	110	0	1.2	501 ²	No	Mixing	Yes	332	110	0.5	0.5	501 ²	No	Mixing	Yes
270	110	0	1.3	501 ²	No	Mixing	Yes	333	110	0.5	1	501 ²	Yes	Mixing	Yes
271	110	0	1.4	501 ²	No	Mixing	No	334	110	0.5	1.1	501 ²	Yes	Mixing	Yes
272	110	0	1.5	501 ²	No	Mixing	No	335	110	0.5	1.2	501 ²	Yes	Mixing	Yes
273	110	0	1.6	501 ²	No	Def. melt	No	336	110	0.5	1.3	501 ²	Yes	Mixing	Yes
274	110	0	1.7	501 ²	No	Solid	No	337	110	0.5	1.4	501 ²	Yes	Mixing	No
275	110	0	1.75	501 ²	No	Solid	No	338	110	0.5	1.5	501 ²	Yes	Mixing	No
276	110	0.1	0.1	501 ²	No	Mixing	Yes	339	110	0.5	1.6	501 ²	Yes	Def. melt	No
277	110	0.1	0.5	501 ²	No	Mixing	Yes	340	110	0.5	1.7	501 ²	Yes	Solid	No
278	110	0.1	1	501 ²	Yes	Mixing	Yes	341	110	0.5	1.75	501 ²	Yes	Solid	No
279	110	0.1	1.1	501 ²	Yes	Mixing	Yes	342	110	0.75	0.1	501 ²	No	Mixing	Yes
280	110	0.1	1.2	501 ²	Yes	Mixing	Yes	343	110	0.75	0.5	501 ²	No	Mixing	Yes
281	110	0.1	1.3	501 ²	Yes	Mixing	Yes	344	110	0.75	1	501 ²	Yes	Mixing	Yes
282	110	0.1	1.4	501 ²	Yes	Mixing	No	345	110	0.75	1.1	501 ²	Yes	Mixing	Yes
283	110	0.1	1.5	501 ²	Yes	Mixing	No	346	110	0.75	1.2	501 ²	Yes	Mixing	Yes
284	110	0.1	1.6	501 ²	Yes	Def. melt	No	347	110	0.75	1.3	501 ²	Yes	Mixing	Yes
285	110	0.1	1.7	501 ²	Yes	Solid	No	348	110	0.75	1.4	501 ²	Yes	Mixing	No
286	110	0.1	1.75	501 ²	Yes	Solid	No	349	110	0.75	1.5	501 ²	Yes	Mixing	No
287	110	0.2	0.1	501 ²	No	Mixing	Yes	350	110	0.75	1.6	501 ²	Yes	Def. melt	No
288	110	0.2	0.5	501 ²	No	Mixing	Yes	351	110	0.75	1.7	501 ²	Yes	Solid	No
289	110	0.2	1	501 ²	Yes	Mixing	Yes	352	110	0.75	1.75	501 ²	Yes	Solid	No
290	110	0.2	1.1	501 ²	Yes	Mixing	Yes	353	140	0	0.1	501 ²	No	Mixing	No
291	110	0.2	1.2	501 ²	Yes	Mixing	Yes	354	140	0	0.5	501 ²	No	Mixing	No
292	110	0.2	1.3	501 ²	Yes	Mixing	Yes	355	140	0	1	501 ²	No	Mixing	No
293	110	0.2	1.4	501 ²	Yes	Mixing	No	356	140	0	1.1	501 ²	No	Mixing	No
294	110	0.2	1.5	501 ²	Yes	Mixing	No	357	140	0	1.2	501 ²	No	Mixing	No
295	110	0.2	1.6	501 ²	Yes	Def. melt	No	358	140	0	1.3	501 ²	No	Mixing	No
296	110	0.2	1.7	501 ²	Yes	Solid	No	359	140	0	1.4	501 ²	No	Mixing	No
297	110	0.2	1.75	501 ²	Yes	Solid	No	360	140	0	1.5	501 ²	No	Mixing	No
298	110	0.25	0.1	501 ²	No	Mixing	Yes	361	140	0	1.6	501 ²	No	Mixing	No
299	110	0.25	0.5	501 ²	No	Mixing	Yes	362	140	0	1.7	501 ²	No	Solid	No
300	110	0.25	1	501 ²	Yes	Mixing	Yes	363	140	0	1.75	501 ²	No	Solid	No
301	110	0.25	1.1	501 ²	Yes	Mixing	Yes	364	140	0.1	0.1	501 ²	No	Mixing	No
302	110	0.25	1.2	501 ²	Yes	Mixing	Yes	365	140	0.1	0.5	501 ²	No	Mixing	No
303	110	0.25	1.3	501 ²	Yes	Mixing	Yes	366	140	0.1	1	501 ²	Yes	Mixing	No
304	110	0.25	1.4	501 ²	Yes	Mixing	No	367	140	0.1	1.1	501 ²	Yes	Mixing	No
305	110	0.25	1.5	501 ²	Yes	Mixing	No	368	140	0.1	1.2	501 ²	Yes	Mixing	No
306	110	0.25	1.6	501 ²	Yes	Def. melt	No	369	140	0.1	1.3	501 ²	Yes	Mixing	No
307	110	0.25	1.7	501 ²	Yes	Solid	No	370	140	0.1	1.4	501 ²	Yes	Mixing	No
308	110	0.25	1.75	501 ²	Yes	Solid	No	371	140	0.1	1.5	501 ²	Yes	Mixing	No
309	110	0.3	0.1	501 ²	No	Mixing	Yes	372	140	0.1	1.6	501 ²	Yes	Mixing	No
310	110	0.3	0.5	501 ²	No	Mixing	Yes	373	140	0.1	1.7	501 ²	Yes	Solid	No
311	110	0.3	1	501 ²	Yes	Mixing	Yes	374	140	0.1	1.75	501 ²	Yes	Solid	No
312	110	0.3	1.1	501 ²	Yes	Mixing	Yes	375	140	0.2	0.1	501 ²	No	Mixing	No
313	110	0.3	1.2	501 ²	Yes	Mixing	Yes	376	140	0.2	0.5	501 ²	No	Mixing	No
314	110	0.3	1.3	501 ²	Yes	Mixing	Yes	377	140	0.2	1	501 ²	Yes	Mixing	No
315	110	0.3	1.4	501 ²	Yes	Mixing	No	378	140	0.2	1.1	501 ²	Yes	Mixing	No
316	110	0.3	1.5	501 ²	Yes	Mixing	No	379	140	0.2	1.2	501 ²	Yes	Mixing	No
317	110	0.3	1.6	501 ²	Yes	Def. melt	No	380	140	0.2	1.3	501 ²	Yes	Mixing	No

No.	R_p	ϕ_{init}	t_{form}	GRID	SHELL	THERMOM. REGIME	UNR. CONV.	No.	R_p	ϕ_{init}	t_{form}	GRID	SHELL	THERMOM. REGIME	UNR. CONV.
381	140	0.2	1.4	501 ²	Yes	Mixing	No	444	170	0	1.1	501 ²	No	Mixing	No
382	140	0.2	1.5	501 ²	Yes	Mixing	No	445	170	0	1.2	501 ²	No	Mixing	No
383	140	0.2	1.6	501 ²	Yes	Mixing	No	446	170	0	1.3	501 ²	No	Mixing	No
384	140	0.2	1.7	501 ²	Yes	Solid	No	447	170	0	1.4	501 ²	No	Mixing	No
385	140	0.2	1.75	501 ²	Yes	Solid	No	448	170	0	1.5	501 ²	No	Mixing	No
386	140	0.25	0.1	501 ²	No	Mixing	No	449	170	0	1.6	501 ²	No	Mixing	No
387	140	0.25	0.5	501 ²	No	Mixing	No	450	170	0	1.7	501 ²	No	Solid	No
388	140	0.25	1	501 ²	Yes	Mixing	No	451	170	0	1.75	501 ²	No	Solid	No
389	140	0.25	1.1	501 ²	Yes	Mixing	No	452	170	0.1	0.1	501 ²	No	Mixing	No
390	140	0.25	1.2	501 ²	Yes	Mixing	No	453	170	0.1	0.5	501 ²	No	Mixing	No
391	140	0.25	1.3	501 ²	Yes	Mixing	No	454	170	0.1	1	501 ²	Yes	Mixing	No
392	140	0.25	1.4	501 ²	Yes	Mixing	No	455	170	0.1	1.1	501 ²	Yes	Mixing	No
393	140	0.25	1.5	501 ²	Yes	Mixing	No	456	170	0.1	1.2	501 ²	Yes	Mixing	No
394	140	0.25	1.6	501 ²	Yes	Mixing	No	457	170	0.1	1.3	501 ²	Yes	Mixing	No
395	140	0.25	1.7	501 ²	Yes	Solid	No	458	170	0.1	1.4	501 ²	Yes	Mixing	No
396	140	0.25	1.75	501 ²	Yes	Solid	No	459	170	0.1	1.5	501 ²	Yes	Mixing	No
397	140	0.3	0.1	501 ²	No	Mixing	No	460	170	0.1	1.6	501 ²	Yes	Mixing	No
398	140	0.3	0.5	501 ²	No	Mixing	No	461	170	0.1	1.7	501 ²	Yes	Solid	No
399	140	0.3	1	501 ²	Yes	Mixing	No	462	170	0.1	1.75	501 ²	Yes	Solid	No
400	140	0.3	1.1	501 ²	Yes	Mixing	No	463	170	0.2	0.1	501 ²	No	Mixing	No
401	140	0.3	1.2	501 ²	Yes	Mixing	No	464	170	0.2	0.5	501 ²	No	Mixing	No
402	140	0.3	1.3	501 ²	Yes	Mixing	No	465	170	0.2	1	501 ²	Yes	Mixing	No
403	140	0.3	1.4	501 ²	Yes	Mixing	No	466	170	0.2	1.1	501 ²	Yes	Mixing	No
404	140	0.3	1.5	501 ²	Yes	Mixing	No	467	170	0.2	1.2	501 ²	Yes	Mixing	No
405	140	0.3	1.6	501 ²	Yes	Mixing	No	468	170	0.2	1.3	501 ²	Yes	Mixing	No
406	140	0.3	1.7	501 ²	Yes	Solid	No	469	170	0.2	1.4	501 ²	Yes	Mixing	No
407	140	0.3	1.75	501 ²	Yes	Solid	No	470	170	0.2	1.5	501 ²	Yes	Mixing	No
408	140	0.4	0.1	501 ²	No	Mixing	No	471	170	0.2	1.6	501 ²	Yes	Mixing	No
409	140	0.4	0.5	501 ²	No	Mixing	No	472	170	0.2	1.7	501 ²	Yes	Solid	No
410	140	0.4	1	501 ²	Yes	Mixing	No	473	170	0.2	1.75	501 ²	Yes	Solid	No
411	140	0.4	1.1	501 ²	Yes	Mixing	No	474	170	0.25	0.1	501 ²	No	Mixing	No
412	140	0.4	1.2	501 ²	Yes	Mixing	No	475	170	0.25	0.5	501 ²	No	Mixing	No
413	140	0.4	1.3	501 ²	Yes	Mixing	No	476	170	0.25	1	501 ²	Yes	Mixing	No
414	140	0.4	1.4	501 ²	Yes	Mixing	No	477	170	0.25	1.1	501 ²	Yes	Mixing	No
415	140	0.4	1.5	501 ²	Yes	Mixing	No	478	170	0.25	1.2	501 ²	Yes	Mixing	No
416	140	0.4	1.6	501 ²	Yes	Mixing	No	479	170	0.25	1.3	501 ²	Yes	Mixing	No
417	140	0.4	1.7	501 ²	Yes	Solid	No	480	170	0.25	1.4	501 ²	Yes	Mixing	No
418	140	0.4	1.75	501 ²	Yes	Solid	No	481	170	0.25	1.5	501 ²	Yes	Mixing	No
419	140	0.5	0.1	501 ²	No	Mixing	No	482	170	0.25	1.6	501 ²	Yes	Mixing	No
420	140	0.5	0.5	501 ²	No	Mixing	No	483	170	0.25	1.7	501 ²	Yes	Def. melt	No
421	140	0.5	1	501 ²	Yes	Mixing	No	484	170	0.25	1.75	501 ²	Yes	Solid	No
422	140	0.5	1.1	501 ²	Yes	Mixing	No	485	170	0.3	0.1	501 ²	No	Mixing	No
423	140	0.5	1.2	501 ²	Yes	Mixing	No	486	170	0.3	0.5	501 ²	No	Mixing	No
424	140	0.5	1.3	501 ²	Yes	Mixing	No	487	170	0.3	1	501 ²	Yes	Mixing	No
425	140	0.5	1.4	501 ²	Yes	Mixing	No	488	170	0.3	1.1	501 ²	Yes	Mixing	No
426	140	0.5	1.5	501 ²	Yes	Mixing	No	489	170	0.3	1.2	501 ²	Yes	Mixing	No
427	140	0.5	1.6	501 ²	Yes	Mixing	No	490	170	0.3	1.3	501 ²	Yes	Mixing	No
428	140	0.5	1.7	501 ²	Yes	Solid	No	491	170	0.3	1.4	501 ²	Yes	Mixing	No
429	140	0.5	1.75	501 ²	Yes	Solid	No	492	170	0.3	1.5	501 ²	Yes	Mixing	No
430	140	0.75	0.1	501 ²	No	Mixing	No	493	170	0.3	1.6	501 ²	Yes	Mixing	No
431	140	0.75	0.5	501 ²	No	Mixing	No	494	170	0.3	1.7	501 ²	Yes	Def. melt	No
432	140	0.75	1	501 ²	Yes	Mixing	No	495	170	0.3	1.75	501 ²	Yes	Solid	No
433	140	0.75	1.1	501 ²	Yes	Mixing	No	496	170	0.4	0.1	501 ²	No	Mixing	No
434	140	0.75	1.2	501 ²	Yes	Mixing	No	497	170	0.4	0.5	501 ²	No	Mixing	No
435	140	0.75	1.3	501 ²	Yes	Mixing	No	498	170	0.4	1	501 ²	Yes	Mixing	No
436	140	0.75	1.4	501 ²	Yes	Mixing	No	499	170	0.4	1.1	501 ²	Yes	Mixing	No
437	140	0.75	1.5	501 ²	Yes	Mixing	No	500	170	0.4	1.2	501 ²	Yes	Mixing	No
438	140	0.75	1.6	501 ²	Yes	Mixing	No	501	170	0.4	1.3	501 ²	Yes	Mixing	No
439	140	0.75	1.7	501 ²	Yes	Solid	No	502	170	0.4	1.4	501 ²	Yes	Mixing	No
440	140	0.75	1.75	501 ²	Yes	Solid	No	503	170	0.4	1.5	501 ²	Yes	Mixing	No
441	170	0	0.1	501 ²	No	Mixing	No	504	170	0.4	1.6	501 ²	Yes	Mixing	No
442	170	0	0.5	501 ²	No	Mixing	No	505	170	0.4	1.7	501 ²	Yes	Def. melt	No
443	170	0	1	501 ²	No	Mixing	No	506	170	0.4	1.75	501 ²	Yes	Solid	No

No.	R_p	ϕ_{init}	t_{form}	GRID	SHELL	THERMOM. REGIME	UNR. CONV.
507	170	0.5	0.1	501 ²	No	Mixing	No
508	170	0.5	0.5	501 ²	No	Mixing	No
509	170	0.5	1	501 ²	Yes	Mixing	No
510	170	0.5	1.1	501 ²	Yes	Mixing	No
511	170	0.5	1.2	501 ²	Yes	Mixing	No
512	170	0.5	1.3	501 ²	Yes	Mixing	No
513	170	0.5	1.4	501 ²	Yes	Mixing	No
514	170	0.5	1.5	501 ²	Yes	Mixing	No
515	170	0.5	1.6	501 ²	Yes	Mixing	No
516	170	0.5	1.7	501 ²	Yes	Def. melt	No
517	170	0.5	1.75	501 ²	Yes	Solid	No
518	170	0.75	0.1	501 ²	No	Mixing	No
519	170	0.75	0.5	501 ²	Yes	Mixing	No
520	170	0.75	1	501 ²	Yes	Mixing	No
521	170	0.75	1.1	501 ²	Yes	Mixing	No
522	170	0.75	1.2	501 ²	Yes	Mixing	No
523	170	0.75	1.3	501 ²	Yes	Mixing	No
524	170	0.75	1.4	501 ²	Yes	Mixing	No
525	170	0.75	1.5	501 ²	Yes	Mixing	No
526	170	0.75	1.6	501 ²	Yes	Mixing	No
527	170	0.75	1.7	501 ²	Yes	Def. melt	No
528	170	0.75	1.75	501 ²	Yes	Solid	No
529	200	0	0.1	501 ²	No	Mixing	No
530	200	0	0.5	501 ²	No	Mixing	No
531	200	0	1	501 ²	No	Mixing	No
532	200	0	1.1	501 ²	No	Mixing	No
533	200	0	1.2	501 ²	No	Mixing	No
534	200	0	1.3	501 ²	No	Mixing	No
535	200	0	1.4	501 ²	No	Mixing	No
536	200	0	1.5	501 ²	No	Mixing	No
537	200	0	1.6	501 ²	No	Mixing	No
538	200	0	1.7	501 ²	No	Mixing	No
539	200	0	1.75	501 ²	No	Solid	No
540	200	0.1	0.1	501 ²	No	Mixing	No
541	200	0.1	0.5	501 ²	No	Mixing	No
542	200	0.1	1	501 ²	Yes	Mixing	No
543	200	0.1	1.1	501 ²	Yes	Mixing	No
544	200	0.1	1.2	501 ²	Yes	Mixing	No
545	200	0.1	1.3	501 ²	Yes	Mixing	No
546	200	0.1	1.4	501 ²	Yes	Mixing	No
547	200	0.1	1.5	501 ²	Yes	Mixing	No
548	200	0.1	1.6	501 ²	Yes	Mixing	No
549	200	0.1	1.7	501 ²	Yes	Mixing	No
550	200	0.1	1.75	501 ²	Yes	Solid	No
551	200	0.2	0.1	501 ²	No	Mixing	No
552	200	0.2	0.5	501 ²	No	Mixing	No
553	200	0.2	1	501 ²	Yes	Mixing	No
554	200	0.2	1.1	501 ²	Yes	Mixing	No
555	200	0.2	1.2	501 ²	Yes	Mixing	No
556	200	0.2	1.3	501 ²	Yes	Mixing	No
557	200	0.2	1.4	501 ²	Yes	Mixing	No
558	200	0.2	1.5	501 ²	Yes	Mixing	No
559	200	0.2	1.6	501 ²	Yes	Mixing	No
560	200	0.2	1.7	501 ²	Yes	Mixing	No
561	200	0.2	1.75	501 ²	Yes	Solid	No
562	200	0.25	0.1	501 ²	No	Mixing	No
563	200	0.25	0.5	501 ²	No	Mixing	No
564	200	0.25	1	501 ²	Yes	Mixing	No
565	200	0.25	1.1	501 ²	Yes	Mixing	No
566	200	0.25	1.2	501 ²	Yes	Mixing	No
567	200	0.25	1.3	501 ²	Yes	Mixing	No
568	200	0.25	1.4	501 ²	Yes	Mixing	No
569	200	0.25	1.5	501 ²	Yes	Mixing	No

No.	R_p	ϕ_{init}	t_{form}	GRID	SHELL	THERMOM. REGIME	UNR. CONV.
570	200	0.25	1.6	501 ²	Yes	Mixing	No
571	200	0.25	1.7	501 ²	Yes	Mixing	No
572	200	0.25	1.75	501 ²	Yes	Solid	No
573	200	0.3	0.1	501 ²	No	Mixing	No
574	200	0.3	0.5	501 ²	No	Mixing	No
575	200	0.3	1	501 ²	Yes	Mixing	No
576	200	0.3	1.1	501 ²	Yes	Mixing	No
577	200	0.3	1.2	501 ²	Yes	Mixing	No
578	200	0.3	1.3	501 ²	Yes	Mixing	No
579	200	0.3	1.4	501 ²	Yes	Mixing	No
580	200	0.3	1.5	501 ²	Yes	Mixing	No
581	200	0.3	1.6	501 ²	Yes	Mixing	No
582	200	0.3	1.7	501 ²	Yes	Mixing	No
583	200	0.3	1.75	501 ²	Yes	Solid	No
584	200	0.4	0.1	501 ²	No	Mixing	No
585	200	0.4	0.5	501 ²	No	Mixing	No
586	200	0.4	1	501 ²	Yes	Mixing	No
587	200	0.4	1.1	501 ²	Yes	Mixing	No
588	200	0.4	1.2	501 ²	Yes	Mixing	No
589	200	0.4	1.3	501 ²	Yes	Mixing	No
590	200	0.4	1.4	501 ²	Yes	Mixing	No
591	200	0.4	1.5	501 ²	Yes	Mixing	No
592	200	0.4	1.6	501 ²	Yes	Mixing	No
593	200	0.4	1.7	501 ²	Yes	Mixing	No
594	200	0.4	1.75	501 ²	Yes	Solid	No
595	200	0.5	0.1	501 ²	No	Mixing	No
596	200	0.5	0.5	501 ²	No	Mixing	No
597	200	0.5	1	501 ²	Yes	Mixing	No
598	200	0.5	1.1	501 ²	Yes	Mixing	No
599	200	0.5	1.2	501 ²	Yes	Mixing	No
600	200	0.5	1.3	501 ²	Yes	Mixing	No
601	200	0.5	1.4	501 ²	Yes	Mixing	No
602	200	0.5	1.5	501 ²	Yes	Mixing	No
603	200	0.5	1.6	501 ²	Yes	Mixing	No
604	200	0.5	1.7	501 ²	Yes	Mixing	No
605	200	0.5	1.75	501 ²	Yes	Solid	No
606	200	0.75	0.1	501 ²	No	Mixing	No
607	200	0.75	0.5	501 ²	No	Mixing	No
608	200	0.75	1	501 ²	Yes	Mixing	No
609	200	0.75	1.1	501 ²	Yes	Mixing	No
610	200	0.75	1.2	501 ²	Yes	Mixing	No
611	200	0.75	1.3	501 ²	Yes	Mixing	No
612	200	0.75	1.4	501 ²	Yes	Mixing	No
613	200	0.75	1.5	501 ²	Yes	Mixing	No
614	200	0.75	1.6	501 ²	Yes	Mixing	No
615	200	0.75	1.7	501 ²	Yes	Mixing	No
616	200	0.75	1.75	501 ²	Yes	Solid	No

Table B.4: List of all 3D simulations with radius R_p (km), formation time t_{form} (Myr) and initial porosity ϕ_{init} (non-dim.). GRID specifies the number of nodes in the finite-difference grid, SHELL indicates whether the corresponding model retained a porous shell after its thermo-mechanical evolution ended and THERMOM. REGIME indicates the evolutionary channel of the model.

No.	R_p	ϕ_{init}	t_{form}	GRID	SHELL	THERMOM. REGIME
617	20	0.4	0.1	261 ³	Yes	Static melt
618	50	0.3	1.75	261 ³	Yes	Solid
619	50	0.3	1.75	261 ³	Yes	Solid
620	50	0.25	0.5	261 ³	No	Def. melt
621	50	0.25	1.5	261 ³	Yes	Static melt
622	50	0.5	1.5	261 ³	Yes	Static melt
623	110	0.25	0.1	261 ³	No	Mixing
624	110	0.25	1.7	261 ³	No	Static melt

No.	R_P	ϕ_{init}	t_{form}	GRID	SHELL	THERMOM. REGIME
625	140	0.2	0.5	261 ³	No	Mixing
626	140	0.4	1.0	261 ³	No	Mixing
627	170	0.4	1.3	261 ³	No	Mixing

Table B.5: List of all 2D simulations of thermo-mechanical type *static melt*, for which the numerical model is consistent with the analytical solution. Parameters are radius R_P (km), formation time t_{form} (Myr), initial porosity ϕ_{init} (non-dim.), GRID specifies the number of nodes in the finite-difference grid, SHELL indicates whether the corresponding model retained a porous shell after its thermo-mechanical evolution.

No.	R_P	ϕ_{init}	t_{form}	GRID	SHELL
003	20	0	1	501 ²	No
004	20	0	1.1	501 ²	No
005	20	0	1.2	501 ²	No
015	20	0.1	1.1	501 ²	Yes
016	20	0.1	1.2	501 ²	Yes
017	20	0.1	1.3	501 ²	Yes
026	20	0.2	1.1	501 ²	Yes
027	20	0.2	1.2	501 ²	Yes
028	20	0.2	1.3	501 ²	Yes
037	20	0.25	1.1	501 ²	Yes
038	20	0.25	1.2	501 ²	Yes
039	20	0.25	1.3	501 ²	Yes
048	20	0.3	1.1	501 ²	Yes
049	20	0.3	1.2	501 ²	Yes
050	20	0.3	1.3	501 ²	Yes
059	20	0.4	1.1	501 ²	Yes
060	20	0.4	1.2	501 ²	Yes
061	20	0.4	1.3	501 ²	Yes
071	20	0.5	1.2	501 ²	Yes
072	20	0.5	1.3	501 ²	Yes
082	20	0.75	1.2	501 ²	Yes
083	20	0.75	1.3	501 ²	Yes
095	50	0	1.4	501 ²	No
096	50	0	1.5	501 ²	No
106	50	0.1	1.4	501 ²	Yes
107	50	0.1	1.5	501 ²	Yes
117	50	0.2	1.4	501 ²	Yes
118	50	0.2	1.5	501 ²	Yes
128	50	0.25	1.4	501 ²	Yes
129	50	0.25	1.5	501 ²	Yes
139	50	0.3	1.4	501 ²	Yes
140	50	0.3	1.5	501 ²	Yes
150	50	0.4	1.4	501 ²	Yes
151	50	0.4	1.5	501 ²	Yes
161	50	0.5	1.4	501 ²	Yes
162	50	0.5	1.5	501 ²	Yes
172	50	0.75	1.4	501 ²	Yes
173	50	0.75	1.5	501 ²	Yes
185	80	0	1.6	501 ²	No
196	80	0.1	1.6	501 ²	Yes
207	80	0.2	1.6	501 ²	Yes
218	80	0.25	1.6	501 ²	Yes
229	80	0.3	1.6	501 ²	Yes
240	80	0.4	1.6	501 ²	Yes
251	80	0.5	1.6	501 ²	Yes
262	80	0.75	1.6	501 ²	Yes

References

References

Abramov, O., Mojzsis, S. J., 2011. Abodes for life in carbonaceous asteroids? *Icarus* 213, 273–279.

- Ahrens, J., Geveci, B., Law, C., 2005. Paraview: An end-user tool for large-data visualization. Elsevier, ISBN-13: 978-0123875822, 2005.
- Barr, A. C., Canup, R. M., 2008. Constraints on gas giant satellite formation from the interior states of partially differentiated satellites. *Icarus* 198, 163–177.
- Barshay, S. S., Lewis, J. S., 1976. Chemistry of primitive solar material. *ARA&A* 14, 81–94.
- Bottinga, Y., Weill, D. F., 1972. The viscosity of magmatic silicate liquids: a model calculation. *Am. J. Sci.* 272, 438–475.
- Chambers, J. E., 2010. Planetesimal formation by turbulent concentration. *Icarus* 208, 505–517.
- Ciesla, F. J., Mulders, G. D., Pascucci, I., Apai, D., 2015. Volatile delivery to planets from water-rich planetesimals around low mass stars. *ApJ* 804, 9.
- Cobb, A. K., Pudritz, R. E., 2014. Nature’s Starships. I. Observed Abundances and Relative Frequencies of Amino Acids in Meteorites. *ApJ* 783, 140–152.
- Cobb, A. K., Pudritz, R. E., Pearce, B. K. D., 2015. Nature’s Starships. II: Simulating the Synthesis of Amino Acids in Meteorite Parent Bodies. *ApJ* 809, 6.
- Costa, A., Caricchi, L., Bagdassarov, N., 2009. A model for the rheology of particle-bearing suspensions and partially molten rocks. *Geochem. Geophys. Geosys* 10, 3010.
- Cramer, F., Schmeling, H., Golabek, G. J., Duret, T., Orendt, R., Buitter, S. J. H., May, D. A., Kaus, B. J. P., Gerya, T. V., Tackley, P. J., 2012. A comparison of numerical surface topography calculations in geodynamic modelling: an evaluation of the ‘sticky air’ method. *Geophys. J. Int.* 189, 38–54.
- Cuzzi, J. N., Hogan, R. C., Shariff, K., 2008. Toward Planetesimals: Dense Chondrule Clumps in the Protoplanetary Nebula. *ApJ* 687, 1432–1447.
- Davison, T. M., O’Brien, D. P., Ciesla, F. J., Collins, G. S., 2013. The early impact histories of meteorite parent bodies. *Meteorit. Planet. Sci.* 48, 1894–1918.
- Dullemond, C. P., Stammler, S. M., Johansen, A., 2014. Forming Chondrules in Impact Splashes. I. Radiative Cooling Model. *ApJ* 794, 91–103.
- Elkins-Tanton, L. T., Weiss, B. P., Zuber, M. T., 2011. Chondrites as samples of differentiated planetesimals. *Earth Planet. Sci. Lett.* 305, 1–10.
- Elser, S., Meyer, M. R., Moore, B., 2012. On the origin of elemental abundances in the terrestrial planets. *Icarus* 221, 859–874.
- Fu, R. R., Elkins-Tanton, L. T., 2014. The fate of magmas in planetesimals and the retention of primitive chondritic crusts. *Earth Planet. Sci. Lett.* 390, 128–137.
- Gail, H.-P., Henke, S., Trieloff, M., 2015. Thermal evolution and sintering of chondritic planetesimals. II. Improved treatment of the compaction process. *A&A* 576, A60.
- Gerya, T. V., Yuen, D. A., 2003. Characteristics-based marker-in-cell method with conservative finite-differences schemes for modeling geological flows with strongly variable transport properties. *Phys. Earth Planet. Int.* 140, 293–318.
- Gerya, T. V., Yuen, D. A., 2007. Robust characteristics method for modelling multiphase visco-elasto-plastic thermo-mechanical problems. *Phys. Earth Planet. Int.* 163, 83–105.
- Ghosh, A., McSween, H. Y., 1998. A Thermal Model for the Differentiation of Asteroid 4 Vesta, Based on Radiogenic Heating. *Icarus* 134, 187–206.
- Golabek, G. J., Bourdon, B., Gerya, T. V., 2014. Numerical models of the thermo-mechanical evolution of planetesimals: Application to the acapulcoite-lodranite parent body. *Meteorit. Planet. Sci.* 49, 1083–1099.
- Golabek, G. J., Keller, T., Gerya, T. V., Zhu, G., Tackley, P. J., Connolly, J. A. D., 2011. Origin of the martian dichotomy and Tharsis from a giant impact causing massive magmatism. *Icarus* 215, 346–357.
- Goldreich, P., Lithwick, Y., Sari, R., 2004. Planet Formation by Coagulation: A Focus on Uranus and Neptune. *ARA&A* 42, 549–601.
- Greenberg, R., Hartmann, W. K., Chapman, C. R., Wacker, J. F., 1978. Planetesimals to planets - Numerical simulation of collisional evolution. *Icarus* 35, 1–26.
- Henke, S., Gail, H.-P., Trieloff, M., Schwarz, W. H., Kleine, T., 2012. Thermal evolution and sintering of chondritic planetesimals. *A&A* 537, A45.
- Herzberg, C., Raterron, P., Zhang, J., 2000. New experimental observations on the anhydrous solidus for peridotite KLB-1. *Geochem. Geophys. Geosyst.* 1, 1051–14.
- Hevey, P. J., Sanders, I. S., 2006. A model for planetesimal meltdown by ²⁶Al and its implications for meteorite parent bodies. *Meteorit. Planet. Sci.* 41, 95–106.

- Howard, L. N., 1964. Convection at high Rayleigh number. Proceedings of the 11th International Congress in Applied Mechanics. Springer, Berlin, pp. 1109–1115.
- Hunter, J. D., 2007. Matplotlib: A 2d graphics environment. Computing In Science & Engineering 9, 90–95.
- Jacobsen, B., Yin, Q.-Z., Moynier, F., Amelin, Y., Krot, A. N., Nagashima, K., Hutcheon, I. D., Palme, H., 2008. ^{26}Al - ^{26}Mg and ^{207}Pb - ^{206}Pb systematics of Allende CAIs: Canonical solar initial $^{26}\text{Al}/^{27}\text{Al}$ ratio reinstated. Earth Planet. Sci. Lett. 272, 353–364.
- Johansen, A., Mac Low, M.-M., Lacerda, P., Bizzarro, M., 2015. Growth of asteroids, planetary embryos, and Kuiper belt objects by chondrule accretion. Sci. Adv. 1, 1500109.
- Johansen, A., Oishi, J. S., Mac Low, M.-M., Klahr, H., Henning, T., Youdin, A., 2007. Rapid planetesimal formation in turbulent circumstellar disks. Nature 448, 1022–1025.
- Jutzi, M., Benz, W., Michel, P., 2008. Numerical simulations of impacts involving porous bodies: I. implementing sub-resolution porosity in a 3d sph hydrocode. Icarus 198, 242–255.
- Jutzi, M., Michel, P., Hiraoka, K., Nakamura, A. M., Benz, W., 2009. Numerical simulations of impacts involving porous bodies: II. comparison with laboratory experiments. Icarus 201, 802–813.
- Kleine, T., Touboul, M., Bourdon, B., Nimmo, F., Mezger, K., Palme, H., Jacobsen, S. B., Yin, Q.-Z., Halliday, A. N., 2009. Hf-W chronology of the accretion and early evolution of asteroids and terrestrial planets. Geochim. Cosmochim. Acta 73, 5150–5188.
- Kraichnan, R. H., 1962. Turbulent Thermal Convection at Arbitrary Prandtl Number. Phys. Fluids 5, 1374–1389.
- Liebske, C., Schmickler, B., Terasaki, H., Poe, B. T., Suzuki, A., Funakoshi, K.-I., Ando, R., Rubie, D. C., 2005. Viscosity of peridotite liquid up to 13 GPa: Implications for magma ocean viscosities. Earth Planet. Sci. Lett. 240, 589–604.
- Mackwell, S. J., 1991. High-temperature rheology of enstatite: Implications for creep in the mantle. Geophys. Res. Lett. 18, 2027–2030.
- Mishra, R. K., Marhas, K. K., Sameer, Feb. 2016. Abundance of ^{60}Fe inferred from nanoSIMS study of QUE 97008 (L3.05) chondrules. Earth Planet. Sci. Lett. 436, 71–81.
- Morbidelli, A., Bottke, W. F., Nesvorný, D., Levison, H. F., 2009. Asteroids were born big. Icarus 204, 558–573.
- Morbidelli, A., Lambrechts, M., Jacobson, S., Bitsch, B., 2015. The great dichotomy of the Solar System: Small terrestrial embryos and massive giant planet cores. Icarus 258, 418–429.
- Neumann, W., Breuer, D., Spohn, T., 2014. Modelling of compaction in planetesimals. A&A 567, A120.
- Parker, R. J., Church, R. P., Davies, M. B., Meyer, M. R., 2014. Supernova enrichment and dynamical histories of solar-type stars in clusters. MNRAS 437, 946–958.
- Parker, R. J., Dale, J. E., 2016. Did the Solar system form in a sequential triggered star formation event? MNRAS 456, 1066–1072.
- Pinkerton, H., Stevenson, R. J., 1992. Methods of determining the rheological properties of magmas at sub-liquidus temperatures. J. Volcanol. Geotherm. Res. 53, 47–66.
- Qin, L., Dauphas, N., Wadhwa, M., Masarik, J., Janney, P. E., 2008. Rapid accretion and differentiation of iron meteorite parent bodies inferred from ^{182}Hf - ^{182}W chronometry and thermal modeling. Earth Planet. Sci. Lett. 273, 94–104.
- Ranalli, G., 1995. Rheology of the Earth. Chapman and Hall, New York.
- Roberts, P. H., 1967. Convection in horizontal layers with internal heat generation. Theory. Fluid Mech. 30, 33–49.
- Rubie, D. C., Melosh, H. J., Reid, J. E., Liebske, C., Righter, K., 2003. Mechanisms of metal-silicate equilibration in the terrestrial magma ocean. Earth Planet. Sci. Lett. 205, 239–255.
- Sahijpal, S., Soni, P., Gupta, G., 2007. Numerical simulations of the differentiation of accreting planetesimals with ^{26}Al and ^{60}Fe as the heat sources. Meteorit. Planet. Sci. 42, 1529–1548.
- Sanders, I. S., Scott, E. R. D., 2012. The origin of chondrules and chondrites: Debris from low-velocity impacts between molten planetesimals? Meteorit. Planet. Sci. 47, 2170–2192.
- Sanders, I. S., Taylor, G. J., 2005. Implications of ^{26}Al in Nebular Dust: Formation of Chondrules by Disruption of Molten Planetesimals. In: Krot, A. N., Scott, E. R. D., Reipurth, B. (Eds.), Chondrites and the Protoplanetary Disk. Vol. 341 of Astronomical Society of the Pacific Conference Series. pp. 915–932.
- Schmeling, H., Babeyko, A. Y., Enns, A., Faccenna, C., Funicello, F., Gerya, T., Golabek, G. J., Grigull, S., Kaus, B. J. P., Morra, G., Schmalholz, S. M., van Hunen, J., 2008. A benchmark comparison of spontaneous subduction models-Towards a free surface. Phys. Earth Planet. Int. 171, 198–223.
- Schubert, G., Spohn, T., Reynolds, R. T., 1986. Thermal histories, compositions and internal structures of the moons of the solar system. In: Satellites. Arizona University Press, pp. 224–292.
- Siggia, E. D., 1994. High Rayleigh number convection. Annu. Rev. Fluid Mech. 26, 137–168.
- Solomatov, V. S., 2015. Magma oceans and primordial mantle differentiation. Treatise on Geophysics 2nd ed., pp. 81–104.
- Sotin, C., Labrosse, S., 1999. Three-dimensional thermal convection in an isoviscous, infinite prandtl number fluid heated from within and from below: applications to the transfer of heat through planetary mantles. Phys. Earth Planet. Int. 112, 171–190.
- Stolper, E., Hager, B. H., Walker, D., Hays, J. F., 1981. Melt segregation from partially molten source regions - The importance of melt density and source region size. J. Geophys. Res. 86, 6261–6271.
- Suzuki, A., Ohtani, E., Kato, T., 1998. Density and thermal expansion of a peridotite melt at high pressure. Phys. Earth Planet. Int. 107, 53–61.
- Tackley, P. J., Schubert, G., Glatzmaier, G. A., Schenk, P., Ratcliff, J. T., Matas, J.-P., 2001. Three-Dimensional Simulations of Mantle Convection in Io. Icarus 149, 79–93.
- Tang, H., Dauphas, N., 2012. Abundance, distribution, and origin of ^{60}Fe in the solar protoplanetary disk. Earth Planet. Sci. Lett. 359, 248–263.
- Tarduno, J. A., Cottrell, R. D., Nimmo, F., Hopkins, J., Voronov, J., Erickson, A., Blackman, E., Scott, E. R. D., McKinley, R., 2012. Evidence for a Dynamo in the Main Group Pallasite Parent Body. Science 338, 939–942.
- Thrane, K., Bizzarro, M., Baker, J. A., 2006. Extremely Brief Formation Interval for Refractory Inclusions and Uniform Distribution of ^{26}Al in the Early Solar System. ApJ 646, L159–L162.
- Tkalcec, B. J., Brenker, F. E., 2014. Plastic deformation of olivine-rich diogenites and implications for mantle processes on the diogenite parent body. Meteorit. Planet. Sci. 49, 1202–1213.
- Tkalcec, B. J., Golabek, G. J., Brenker, F. E., 2013. Solid-state plastic deformation in the dynamic interior of a differentiated asteroid. Nature Geosci. 6, 93–97.
- Trønnes, R. G., Frost, D. J., 2002. Peridotite melting and mineral-melt partitioning of major and minor elements at 22–24.5 GPa. Earth Planet. Sci. Lett. 197, 117–131.
- Turcotte, D. L., Schubert, G., 2014. Geodynamics, 3rd ed. Cambridge University Press, p. 636.
- Wade, J., Wood, B. J., 2005. Core formation and the oxidation state of the Earth. Earth Planet. Sci. Lett. 236, 78–95.
- Weidenschilling, S. J., 1977. Aerodynamics of solid bodies in the solar nebula. MNRAS 180, 57–70.
- Weidenschilling, S. J., Cuzzi, J. N., 2006. Accretion Dynamics and Timescales: Relation to Chondrites. Meteorites and the Early Solar System II, 1. pp. 473–485.
- Weiss, B. P., Elkins-Tanton, L. T., 2013. Differentiated Planetesimals and the Parent Bodies of Chondrites. Annu. Rev. Earth Planet. Sci. 41, 529–560.
- Yomogida, K., Matsui, T., 1984. Multiple parent bodies of ordinary chondrites. Earth Planet. Sci. Lett. 68, 34–42.
- Zsom, A., Ormel, C. W., Güttler, C., Blum, J., Dullemond, C. P., 2010. The outcome of protoplanetary dust growth: pebbles, boulders, or planetesimals? II. Introducing the bouncing barrier. A&A 513, A57.